

Finite element models for coupled magma/mantle dynamics with anisotropic viscosity

Sjoerd Hack

October 3, 2014

1 Introduction

Partially molten rocks consist of a matrix of solid grains with magma flowing through the pores. It is known from experiments that under the application of a shear stress the solid matrix and magma segregate and form a banded structure Spiegelman [2003]. This is called the growth of porosity perturbations, where the porosity is the fraction of the magma. The study of these porosity perturbations is performed in the framework of the theory of coupled magma/mantle dynamics Katz and Spiegelman [2013]. However this theory predicts that the porosity bands are aligned at $\pi/4$ radians to the shear plane, and in the experiments the perturbation angle is $\pi/9$. The theory of anisotropic viscosity has been developed to explain this lower angle Takei and Katz [2013]. It gives a correct prediction of the lower perturbation angle in simple shear flow. However further testing of the hypothesis of viscous anisotropy is required. One possibility for further testing is to consider torsional flow experiments Qi et al. [2013] Qi et al. [2014]. The theory of anisotropic viscosity makes the novel prediction of the existence of so-called base-state segregation. This is segregation of the liquid and the solid at the scale of the domain, in other words the radius of the cylinder. Base-state segregation can interact with the growth of porosity perturbations through various nonlinearities. The original objective of this project was to perform additional validation of the theory of anisotropic viscosity by comparison of numerical simulations to laboratory experiments. In Katz and Takei [2013] numerical simulations are performed for torsional flow. However these have been performed in cylindrical coordinates and this results in a variable mesh-spacing at the axis of the cylinder. This leads to a bias in the growth rate of porosity perturbations. This problem can be avoided by the use of cartesian coordinates, which is what this project sets out to do. Additionally the mesh size was too low in Katz and Takei [2013]. Perturbation growth in torsional flow is a phenomenon that is inherently three-dimensional. Also there is large difference in the domain-wide length scale of base-state segregation and the very small length scale of the porosity perturbation. The simulation needs to resolve either of these length scales. This results in a very large mesh. The iterative solver used in Katz and Takei [2013] was not fast enough to solve the linear system of equations resulting from a very large mesh size. Fortunately a good preconditioner for a finite-element model of coupled magma/mantle dynamics has been developed Rhebergen et al. [2014]. The objective of this project is to implement viscous anisotropy into this finite-element model and to perform simulations with a high mesh size of torsional flow.

2 Problem formulation

2.1 Dimensional conservation equations

Partially molten rocks consist of a matrix of solid grains with magma flowing through the pores. The theory of coupled magma/mantle dynamics models partially molten rocks at the continuum level as a two-phase fluid with the magma and matrix as co-existing liquid and solid phases respectively. These permeate the entire domain, with the variable porosity representing the volume fraction of magma. The governing equations are derived from the principles of conservation of mass and momentum. The Reynolds number is assumed to be very low. In other words the viscous terms dominate the inertial terms. This means that the expressions of conservation of momentum reduce to expressions of stress balance. In contrast to Darcy flow, the solid can be deformed by shear stresses. At the scale of individual grains and pores the solid grains and the magma are incompressible. However at the aggregate level the solid and the liquid phase can sustain a volumetric strain rate which represents the physical mechanism of compaction. The governing equations were introduced by McKenzie [1984] and can be solved for the pressure p_f , solid velocity \mathbf{u}_s , the liquid velocity \mathbf{u}_f and the porosity ϕ , which represents the volume fraction of the magma at the continuum level. The subscript f in the symbol p_f for the pressure refers to liquid, and this variable is often called the liquid pressure. One should not read too much into this. If the solid is not deforming then its normal stress components equal the pressure p_f , and we do not solve for a separate solid pressure. A short derivation of the conservation equations is given in the appendix. They are given by

$$\partial_t \phi - \nabla \cdot ((1 - \phi)\mathbf{u}_s) = 0, \quad (1a)$$

$$\nabla \cdot (\mathbf{u}_s + \mathbf{q}) = 0, \quad (1b)$$

$$\mathbf{q} = -\frac{k_\phi}{\mu} (\nabla p_f + \rho_f g z), \quad (1c)$$

$$0 = \frac{\partial}{\partial x_j} (\sigma_{ij}) + \rho g_i, \quad (1d)$$

where k_ϕ is the permeability at the aggregate level, μ is the viscosity of the magma at the scale of individual grains and pores, ρ is the phase-averaged density, g is the gravitational constant, σ_{ij} is the stress tensor of the solid+liquid aggregate (tension positive)

$$\sigma_{ij} = (1 - \phi)\sigma_{ij}^s + \phi\sigma_{ij}^f, \quad (2)$$

and \mathbf{q} is the phase separation flux

$$\mathbf{q} = \phi(\mathbf{u}_f - \mathbf{u}_s). \quad (3)$$

The first equation represents mass conservation for the solid phase and describes how the porosity is advected by the solid velocity; the second equation represents mass conservation for the the two-phase (bulk) aggregate; the third equation is the stress balance for the liquid phase and can be seen as a modified Darcy's law; the fourth equation is the stress balance for the two-phase aggregate and is related to the Stokes equation. In the derivation of the liquid stress balance a constitutive relation for the liquid stress tensor has already been applied. Application of constitutive relations to the bulk stress balance has been delayed because the theory of anisotropic viscosity makes a modification here. This modification will be discussed shortly but first preliminary constitutive equations will be applied and the equations will be written in a simplified form. Constitutive relations are also required for the various coefficients. The viscosity of the magma at the scale of individual pores and grains μ is assumed to be constant. The constitutive relation for k_ϕ is described in Rhebergen et al. [2014]. The solid stress tensor depends on the solid strain rate tensor through a fourth-order viscosity tensor

$$\sigma_{ij}^s = -p_f \delta_{ij} + C_{ijkl} \dot{\epsilon}_{kl}. \quad (4)$$

In coupled magma/mantle dynamics the viscosity tensor is usually assumed to be isotropic and simplified to an expression that depends on only two components. However in the theory of anisotropic viscosity a more complicated viscosity tensor is used that will be described shortly. So far equation 4 is only an incomplete constitutive equation. The liquid is unable to sustain shear stresses. Its stress tensor is given by

$$\sigma_{ij}^f = -p_f \delta_{ij}. \quad (5)$$

Substituting the definitions of the solid and liquid stress tensor into the definition of the bulk stress tensor 6 results in the following incomplete constitutive equation for the bulk stress tensor and the solid strain rate tensor

$$\sigma_{ij} = -p_f \delta_{ij} + (1 - \phi) C_{ijkl} \dot{e}_{kl}. \quad (6)$$

It can be inferred from the system of conservation equations 1a-1d and the incomplete constitutive equation for the bulk stress tensor 6 that the liquid velocity can be obtained directly from the solid velocity using the liquid stress balance 1c. It is therefore unnecessary to solve for the liquid velocity together with the other variables and it can be eliminated from the equations. In this report the conservation equations will be applied to models of 2D simple shear flow and 3D torsional flow. In these models the gravity terms are neglected. These modifications result in the following system of conservation equations

$$\partial_t \phi - \nabla \cdot ((1 - \phi) \mathbf{u}_s) = 0, \quad (7a)$$

$$\nabla \cdot \mathbf{u}_s = \nabla \cdot \left(\frac{k_\phi}{\mu} \nabla p_f \right) \quad (7b)$$

$$0 = \frac{\partial}{\partial x_j} (-p_f \delta_{ij} + (1 - \phi) C_{ijkl} \dot{e}_{kl}), \quad (7c)$$

The second equation is called the compaction equation. So far the bulk stress tensor has been related to the solid strain rate tensor through a fourth-order viscosity tensor. A fourth-order tensor has 81 components. In fluid mechanics the viscosity tensor is usually assumed to be isotropic. Additionally symmetry of the stress tensor and strain rate tensor is applied. With these assumptions it can be shown that only two independent components of the viscosity tensor remain. In the theory of anisotropic viscosity this assumption is relaxed Takei and Katz [2013]. Under viscous isotropy the tensile or compressive stress in some direction depends on the scalar volumetric strain rate and on the elongation or contraction rate in this particular direction. Under viscous anisotropy the elongation or contraction rate in the direction of anisotropy has a diminished effect on the tensile or compressive stress in this direction. Under saturated anisotropy it has no effect at all. The theory of anisotropic viscosity makes a distinction between the regimes of fixed and dynamic anisotropy. In the physically realistic case of dynamic anisotropy the anisotropy direction coincides with the direction of maximum tensile stress and the anisotropy magnitude depends on the difference between the maximum and the minimum tensile stress. In the model regime of fixed anisotropy the anisotropy direction and magnitude are fixed. The dimensional viscosity tensor in grain coordinates is given by

$$C_{ijkl} = \zeta_\phi \delta_{ij} \delta_{kl} + \eta_\phi (\delta_{ik} \delta_{jl} + \delta_{il} \delta_{jk} - \frac{2}{3} \delta_{ij} \delta_{kl}) - \Delta \delta_{ix_g} \delta_{jx_g} \delta_{kx_g} \delta_{lx_g}. \quad (8)$$

Here ζ_ϕ is the bulk viscosity, η_ϕ is the shear viscosity and Δ is the anisotropy magnitude. Note that these are variables that refer to the aggregate level. Constitutive equations for ζ_ϕ and η_ϕ are specified in Rhebergen et al. [2014]. They will be described in the section about nondimensionalisation. The term grain coordinates refers to the fact that viscous anisotropy

arises from anisotropy in the distribution of contact area between adjacent solid grains. Under fixed anisotropy the grain coordinates refer to a coordinate system where x_g is aligned with the anisotropy direction. Under dynamic anisotropy the grain coordinates are aligned with the principal moments of the stress tensor. The anisotropy magnitude is assumed to be proportional to the shear viscosity

$$\Delta = \alpha\eta_\phi. \quad (9)$$

In the remainder of this report α will be referred to as the anisotropy magnitude. Saturated anisotropy corresponds to $\alpha = 2.0$. Substituting the viscosity tensor into the bulk stress balance and writing out all the terms except the anisotropy term in vector notation gives

$$\nabla p_f = \nabla((1-\phi)(\zeta_\phi - \frac{2}{3}\eta_\phi)\nabla \cdot \mathbf{u}_s) + \nabla((1-\phi)\eta_\phi(\nabla \mathbf{u}_s + \nabla \mathbf{u}_s^T)) - \frac{\partial}{\partial x_j}((1-\phi)\alpha\eta_\phi\delta_{ix_g}\delta_{jx_g}\delta_{kx_g}\delta_{lx_g}\dot{e}_{kl}). \quad (10)$$

This equation is clearly related to the Stokes equation with the addition of a term representing compaction stresses and an anisotropy term.

2.2 Nondimensional conservation equations

The equations will be nondimensionalized with the following general scaling

$$\mathbf{u}_s = u_0\mathbf{u}_s^*, \quad (11a)$$

$$\mathbf{x} = H\mathbf{x}^*, \quad (11b)$$

$$p_f = p_f^* \frac{\eta_0 u_0}{H}, \quad (11c)$$

$$t = (H/u_0)t^*, \quad (11d)$$

$$k_\phi = k_0 k_\phi^*, \quad (11e)$$

$$\dot{e}_{kl} = (u_0/H)\dot{e}_{kl}^*, \quad (11f)$$

$$\eta_\phi = \eta_0 \eta_\phi^*, \quad (11g)$$

$$\zeta_\phi = \eta_0 r_\zeta \zeta_\phi^*. \quad (11h)$$

Here the variables with stars are the nondimensionalized variables. u_0 is the characteristic velocity. In 3D torsional flow a suitable characteristic velocity is $u_0 = \dot{\psi}H$ where $\dot{\psi}$ is the twist rate and H is the length of the cylinder. For 2D simple shear flow a suitable characteristic velocity is $u_0 = \dot{\gamma}H$, where $\dot{\gamma}$ is the strain rate and H is the height of the domain. η_0 and k_0 are the characteristic shear viscosity and permeability respectively. r_ζ is the bulk/shear viscosity ratio. The term bulk/shear viscosity refers to the fact that in Takei and Katz [2013] the bulk viscosity is proportional to the shear viscosity. In Rhebergen et al. [2014] a different porosity-dependence is used for the bulk and the shear viscosity however. The nondimensional version of the bulk stress balance 10 is given by

$$\nabla p_f = \nabla((r_\zeta \zeta_\phi - \frac{2}{3}\eta_\phi)\nabla \cdot \mathbf{u}_s) + \nabla(\eta_\phi(\nabla \mathbf{u}_f + \nabla \mathbf{u}_f^T)) - \frac{\partial}{\partial x_j}(\alpha\eta_\phi\delta_{ix_g}\delta_{jx_g}\delta_{kx_g}\delta_{lx_g}\dot{e}_{kl}). \quad (12)$$

The star notation has been dropped here. The factor $1 - \phi$ has been absorbed into the shear viscosity. In the code this factor is actually neglected. This is not a problem because the porosity is small $\phi \approx .05$. The nondimensional version of the compaction equation 7b is given by

$$\nabla \cdot \mathbf{u}_s = \nabla(k_\phi \nabla p_f) \frac{k_0 \eta_0}{\mu H^2}. \quad (13)$$

An important length scale in magma/mantle dynamics is the compaction length Katz and Spiegelman [2013]

$$\delta_c = \sqrt{\left(\frac{r_\zeta + 4/3}{\mu}\right)\eta_0 k_0}. \quad (14)$$

The factor of coefficients on the right-hand side of the nondimensional compaction equation 13 can be written in terms of the nondimensional compaction length $R = \delta_c/H$

$$\frac{k_0\eta_0}{\mu H^2} = \frac{R^2}{r_\zeta + \frac{4}{3}}. \quad (15)$$

Following Rhebergen et al. [2014] I will now redefine the permeability and the shear viscosity

$$k_\phi \leftarrow \frac{R^2}{r_\zeta + 4/3} k_\phi, \quad (16a)$$

$$\eta_\phi \leftarrow 2\eta_\phi, \quad (16b)$$

$$\zeta_\phi \leftarrow r_\zeta \zeta_\phi. \quad (16c)$$

The full system of nondimensional conservation equations is given by

$$\partial_t \phi = \nabla \cdot [(1 - \phi)\mathbf{u}_s], \quad (17a)$$

$$\nabla \cdot \mathbf{u}_s = \nabla \cdot [k_\phi \nabla p_f], \quad (17b)$$

$$\nabla p_f = \nabla \cdot \left(\left(\zeta_\phi - \frac{1}{3}\eta_\phi \right) \nabla \cdot \mathbf{u}_s \right) + \nabla \cdot \left(\frac{1}{2}\eta_\phi (\nabla \mathbf{u}_f + \nabla \mathbf{u}_f^T) \right) - \frac{\partial}{\partial x_j} \left(\frac{1}{2}\alpha\eta_\phi \delta_{ix_g} \delta_{jx_g} \delta_{kx_g} \delta_{lx_g} \dot{e}_{kl} \right). \quad (17c)$$

$$(17d)$$

Note that the equations are at this point still expressed in grain coordinates, where x_g is aligned with the anisotropy direction. We will give the coefficients that have been used. The permeability is given by

$$k_\phi = \frac{R^2}{r_\zeta + 4/3} \left(\frac{\phi}{\phi_0} \right)^2. \quad (18)$$

Here r_ζ is the bulk/shear viscosity ratio $\frac{5}{3}$ and ϕ_0 is the reference porosity 0.05. R is the nondimensional compaction length. The shear viscosity is given by

$$\eta_\phi = 2 \exp(-\lambda(\phi - \phi_0)). \quad (19)$$

λ is the porosity-weakening factor of the shear viscosity. The bulk viscosity is given by

$$\zeta_\phi = r_\zeta \frac{\phi}{\phi_0}^{-1}. \quad (20)$$

2.2.1 Three-field formulation

Grad-div terms result in numerical instability for low values of the porosity ϕ Rhebergen et al. [2014]. This instability can cause the porosity to go out of bounds, as is seen in ???. A solution to this problem is to use a three-field formulation Rhebergen et al. [2014]. Here a new variable p_c is introduced

$$p_c = -\zeta_\phi \nabla \cdot \mathbf{u}_s. \quad (21)$$

It can be seen that this velocity is related to the compaction rate $\nabla \cdot \mathbf{u}_s$. The bulk stress balance is now given by

$$0 = \nabla \cdot \left(-\frac{1}{3}\eta_\phi \nabla \cdot \mathbf{u}_s \right) + \nabla \cdot \left(\frac{1}{2}\eta_\phi (\nabla \mathbf{u}_f + \nabla \mathbf{u}_f^T) \right) - \nabla p_f - \nabla p_c - \frac{\partial}{\partial x_j} \left(\frac{1}{2}\alpha\eta_\phi \delta_{ix_g} \delta_{jx_g} \delta_{kx_g} \delta_{lx_g} \dot{e}_{kl} \right). \quad (22)$$

The definition of the compaction pressure (21) is then added to the system of equations that needs to be solved

$$\partial_t \phi = \nabla \cdot [(1 - \phi) \mathbf{u}_s], \quad (23a)$$

$$\nabla \cdot \mathbf{u}_s = \nabla \cdot [k_\phi \nabla p_f], \quad (23b)$$

$$0 = \nabla \cdot \left(-\frac{1}{3} \eta_\phi \nabla \cdot \mathbf{u}_s \right) + \nabla \cdot \left(\frac{1}{2} \eta_\phi (\nabla \mathbf{u}_f + \nabla \mathbf{u}_f^T) \right) - \nabla p_f - \nabla p_c - \frac{\partial}{\partial x_j} \left(\frac{1}{2} \alpha \eta_\phi \delta_{ix_g} \delta_{jx_g} \delta_{kx_g} \delta_{lx_g} \dot{\epsilon}_{kl} \right), \quad (23c)$$

$$p_c = -\zeta_\phi \nabla \cdot \mathbf{u}_s. \quad (23d)$$

Note that this system of equations is still written in grain coordinates. When we refer to this system of equations in the remainder of this report it is understood that we mean the version in cartesian coordinates.

2.2.2 Time-integration

The system of equations (23) is nonlinear because k_ϕ , η_ϕ and ζ_ϕ are porosity-dependent. Non-linear systems of equations are harder to solve than linear ones. However in this case solving a nonlinear system of equations can be avoided. The time-dependent code that has been used in Katz and Takei [2013] utilizes a staggered scheme where the porosity-advection equation (23a) and the remainder of the equations (23b)-(23d) are solved alternately. For a given value of porosity the compaction equation, modified bulk stress balance and definition of compaction pressure (23b)-(23d) are linear equations that will result in a linear system after discretisation. These equations are sometimes called the elliptic part of the equations (23), even though it will turn out that ellipticity is lost for $\alpha > \frac{4}{3}$ in the 2d simple shear flow case due to the introduction of the compaction pressure. The 3d torsional flow case remains elliptic up to saturated anisotropy. In this report no time-dependent simulations have been run, because there are numerical perturbations in the 3d torsional flow case. These make the quality of the solution so low for small mesh sizes that it is pointless to run time-dependent simulations. That said, some work has been done for the time-dependent code. In the Bitbucket for this project a time-dependent code can be found that fixes a few bugs in the existing time-dependent code. In summary this project is concerned with solving the equations (23b)-(23d) for a fixed porosity field, in which case they are linear.

2.3 Test cases

The objective of this project is to validate of the theory of anisotropic viscosity by comparison of numerical solutions to the experimental results. Experimental results are available for geometries that represent simple shear and torsional deformation.

2.3.1 3D torsional deformation

Validation of the theory in torsional deformation is particularly important because this configuration exhibits the physical phenomenon of base-state segregation which is absent in simple shear flow. In Katz and Takei [2013] numerical solutions for torsional flow are presented but the use of cylindrical coordinates leads to a variable grid-spacing and a bias in the growth rate of porosity perturbations. The use of cartesian coordinates is expected to avoid this bias. It is important to find appropriate boundary conditions for a weak formulation that makes use of cartesian coordinates. In Takei and Katz [2013] the boundary conditions for torsional

deformation are presented in cylindrical coordinates

$$u_r^s = u_\psi^s = u_{z,r}^s, \quad p_{f,r} = 0 \quad \text{at} \quad r = 0, \quad (24a)$$

$$u_{\psi,r}^s = z - 1/2, \quad u_r^s = u_{z,r}^s = 0, \quad k_\phi = 0 \quad \text{at} \quad r = L/H, \quad (24b)$$

$$u_\psi^s = -r/2, \quad u_r^s = u_z^s = 0, \quad k_\phi = 0 \quad \text{at} \quad z = 0, \quad (24c)$$

$$u_\psi^s = r/2, \quad u_r^s = u_z^s = 0, \quad k_\phi = 0 \quad \text{at} \quad z = 1. \quad (24d)$$

L is the dimensional length of the cylinder and H is the dimensional radius. A physical interpretation of the boundary condition for the velocity at the side wall is not available. An attempt has been made to implement these boundary conditions in the code but it has not been completed because a certain functionality is lacking in FEniCS. There is also an alternative way to do it but this will require a considerable amount of analysis. A few notes on this are given in the appendix B.

In the remainder of the report a Dirichlet boundary condition is applied to the velocity. In addition, following Alisic et al. [2013] a Neumann boundary condition is applied to the liquid pressure. The weak formulation does not change as a result of this choice of boundary condition for the liquid pressure. The boundary conditions in cylindrical coordinates are given by

$$u_\psi^s = r(z - 1/2), \quad u_r^s = u_z^s = 0, \quad -k_\phi \nabla p_f \cdot \hat{\mathbf{n}} = 0 \quad \text{at} \quad r = 1, z = 0, z = 1 \quad (25)$$

In cartesian coordinates they are given by

$$u_x^s = -\sin(\psi)r(z - 1/2), \quad (26a)$$

$$u_y^s = \cos(\psi)r(z - 1/2), \quad (26b)$$

$$u_z^s = 0, \quad (26c)$$

$$-k_\phi \nabla p_f \cdot \hat{\mathbf{n}} = 0 \quad \text{at} \quad r = 1, z = 0, z = 1, \quad (26d)$$

where $\psi = \text{atan2}(x, y)$ and $r = \sqrt{(x^2 + y^2)}$. The use of Dirichlet boundary conditions for the velocity has a disadvantage. The code is intended for simulations that consider the growth of spiral-staircase shaped porosity perturbations. These intersect the side boundaries. The use of Dirichlet boundaries prevents growth of the porosity perturbations at the side boundaries because the solid cannot move into and out of the high-porosity bands. This is expected to result in a deviation from the results in Katz and Takei [2013]. Informal tests show that this disturbance does not extend a large distance into the domain. Another consideration to take into account is that the choice of boundary conditions may have implications for the convergence of iterative solvers. In section 3.2 some simulation results are given that illustrate this phenomenon.

In conclusion Dirichlet boundary conditions for the velocity are applied at the side boundaries. These are easy to implement but they are expected to result in a deviation from the results in Katz and Takei [2013] at the side boundaries. Also there may be implications for convergence of the iterative solver, but this is probably a result of other problems in the scheme.

2.3.2 2D simple shear

The boundary conditions for simple shear flow are given by

$$u_x^s = y - \frac{1}{2}, \quad u_y^s = 0 \quad \text{at} \quad y = 0, 1, \quad (27a)$$

$$\text{periodic} \quad \text{at} \quad x = 0, 1. \quad (27b)$$

It is known that the weak formulation that is given in section 2.4 does not change as a result of the introduction of the periodic boundary condition, although this is not shown in this report.

2.4 Summary of weak formulation

The basis of a finite element discretisation is a weak formulation. The weak formulation is given by

$$0 = \int_{\Omega} \eta_{\phi} \mathbf{D}\mathbf{u}_s : \mathbf{D}\mathbf{v} \, dx + \int_{\Omega} (\zeta_{\phi} - \frac{1}{3}\eta_{\phi})(\nabla \cdot \mathbf{u}_s)(\nabla \cdot \mathbf{v}) \, dx \quad (28a)$$

$$- \int_{\Omega} p_f \nabla \cdot \mathbf{v} \, dx - \int_{\Omega} q \nabla \cdot \mathbf{u}_s \, dx - \int_{\Omega} k_{\phi} \nabla p_f \cdot \nabla q \, dx - \int_{\Omega} \frac{\dot{e}_{ij} + \dot{e}_{ji}}{2} \alpha \eta_{\phi} \delta_{ix_g} \delta_{jx_g} \delta_{kx_g} \delta_{lx_g} \dot{e}_{kl} \, dx. \quad (28b)$$

Here q is a scalar-valued test function that corresponds to the liquid pressure and \mathbf{v} is a vector-valued test function that corresponds to the solid velocity. Note that the first strain rate tensor in the anisotropy term refers to the test velocity. A derivation of this weak formulation is given in the appendix A. Essential boundary conditions are boundary conditions that have not been integrated into the integral statement and that need to be explicitly imposed. They result in a modification of the space of test functions. We have the following essential boundary condition

$$\mathbf{u}_s = (0, \frac{r}{2}(z - 1/2), 0) \quad (29)$$

on the side, top and bottom wall of the cylinder. We consider the space of test functions with

$$\mathbf{v} = \mathbf{0} \quad (30)$$

on the top and bottom wall and the side wall. The weak formulation now reads: (\mathbf{u}_s, p_f) is a solution of the weak formulation if it satisfies the integral statement (31) for all test functions (\mathbf{v}, q) that satisfy (30). In the weak formulation we added the weak formulations for the compaction equation and the balance of stresses for the aggregate. This is allowed because q and \mathbf{v} are arbitrary functions in the space of test functions and we can recover the individual weak formulations by substituting $q = 0$ and $\mathbf{v} = \mathbf{0}$.

In the remainder of this section some remarks are given about discretisation of the weak formulation. To find an approximation to \mathbf{u}_s using a computer the weak formulation needs to be discretised. This is called finite element assembly, and it is automated in FEniCS, which is a FEM assembler at heart. One thing that is important here is the choice of elements. The most obvious choice would be to use $P1 - P1$ elements where piecewise linear basis functions are used to approximate the solid velocity and the liquid pressure but this results in numerical instability. Therefore $P2 - P1$ elements are used. The coefficients are interpolated by piecewise quadratic functions, where $\eta_{\phi} a_{i1} a_{j1} a_{k1} a_{l1}$ is seen as a single coefficient. Some variations of this will be considered in the remainder of the report in the examination of numerical instabilities in the 3d torsional flow case.

2.4.1 Weak formulation of the three-field formulation

The weak formulation for the three-field formulation is given by

$$0 = \int_{\Omega} \eta_{\phi} \mathbf{D}\mathbf{u}_s : \mathbf{D}\mathbf{v} \, dx + \int_{\Omega} -\frac{1}{3}\eta_{\phi}(\nabla \cdot \mathbf{u}_s)(\nabla \cdot \mathbf{v}) \, dx \quad (31a)$$

$$- \int_{\Omega} p_f \nabla \cdot \mathbf{v} \, dx - \int_{\Omega} q \nabla \cdot \mathbf{u}_s \, dx - \int_{\Omega} k_{\phi} \nabla p_f \cdot \nabla q \, dx - \int_{\Omega} \frac{\dot{e}_{ij} + \dot{e}_{ji}}{2} \alpha \eta_{\phi} \delta_{ix_g} \delta_{jx_g} \delta_{kx_g} \delta_{lx_g} \dot{e}_{kl} \, dx \quad (31b)$$

$$- \int_{\Omega} p_c \nabla \cdot \mathbf{v} \, dx - \int_{\Omega} \zeta_{\phi} p_c w \, dx - \int_{\Omega} w \nabla \cdot \mathbf{u}_s \, dx. \quad (31c)$$

Here (\mathbf{u}_s, p_f, p_c) are the trial functions we want to solve for, and (\mathbf{v}, q, w) are the corresponding test functions. Note that this weak formulation is still expressed in grain coordinates. The code uses cartesian coordinates. Therefore the weak formulation still needs to be expressed in cartesian coordinates before it can be used in the code.

2.5 Expressing the anisotropy term in cartesian coordinates

The weak formulation (31) is still expressed in grain coordinates. The code uses cartesian coordinates. Therefore the weak formulation still needs to be expressed in cartesian coordinates before it can be used in the code. Vector notation is independent of the coordinate system. This means that the only term that needs to be modified is the anisotropy term. For this we need to express $\delta_{ix_g}\delta_{jx_g}\delta_{kx_g}\delta_{lx_g}\dot{e}_{kl}$ in cartesian coordinates. \dot{e}_{kl} is here given in grain coordinates. We need to express it in cartesian coordinates. This is equivalent to a rotation of the coordinate system. A rotation of the coordinate system can be described by a rotation matrix R that maps the grain coordinates to the cartesian coordinates. The strain rate tensor in the grain coordinates can be expressed in the continuum coordinates in the following way

$$\dot{e} = R^T \tilde{e} R. \quad (32)$$

Here \dot{e} is the strain rate tensor in grain coordinates and \tilde{e} is the strain rate tensor in cartesian coordinates. We are here making use of equation (2.12) in Kundu et al. [2011] and the fact that the primed variables there correspond to the variables in grain coordinates for C_{ij} that maps from grain coordinates to the continuum coordinates. It is now possible to calculate $\delta_{ix_g}\delta_{jx_g}\delta_{kx_g}\delta_{lx_g}(R^T \tilde{e} R)_{kl}$ where \tilde{e} is expressed in cartesian coordinates. The result is still expressed in grain coordinates. It is necessary to express this in cartesian coordinates. The mapping from the continuum coordinates to the grain coordinates is the inverse of the mapping from the grain coordinates to the continuum coordinates R . A rotation matrix R is orthogonal so its inverse is given by its transpose $R^{-1} = R^T$. The anisotropy term in cartesian coordinates then becomes

$$R(\delta_{ix_g}\delta_{jx_g}\delta_{kx_g}\delta_{lx_g}(R^T \tilde{e} R)_{kl})R^T. \quad (33)$$

In the grain coordinates x_g corresponds to the first coordinate direction so this can also be written as

$$R(\delta_{i1}\delta_{j1}\delta_{k1}\delta_{l1}(R^T \tilde{e} R)_{kl})R^T. \quad (34)$$

I think I need to be clear here. We first calculate two matrix products $R^T \tilde{e} R$, then we take the contraction product of the resulting second order tensor and the fourth-order tensor $\delta_{i1}\delta_{j1}\delta_{k1}\delta_{l1}$ and then we calculate two additional matrix products. It can be verified by writing it out in indicial coordinates that (34) is equal to

$$R_{i1}R_{j1}R_{k1}R_{l1}\dot{e}_{kl}, \quad (35)$$

where R is the rotation matrix that maps from the grain coordinates to the cartesian coordinates and \dot{e}_{kl} is the strain rate tensor in cartesian coordinates. This is similar to what has been calculated in equation (3.7) in Katz and Takei [2013]. This expression cannot be simplified any further. We do still need an expression for the rotation matrix. There are multiple cases to consider here. As mentioned the rotation matrix rotates the grain coordinates to the cartesian coordinates. The grain coordinates are a coordinate system where x_g is aligned with the anisotropy direction. Under fixed anisotropy the anisotropy direction is fixed. We will now determine the rotation matrix in 2D simple shear flow and 3D torsional flow. Afterwards we will consider the rotation matrices for complete and incomplete dynamic anisotropy.

2.5.1 Rotation matrix in 2D simple shear flow

The anisotropy direction is aligned at an angle of $\frac{\pi}{4}$ radians to the shear plane. It can be seen that this is the direction of maximum tensile stress for the base-state solution with constant porosity $\phi = .05$. A figure of the configuration with the grain coordinate axes and the cartesian coordinate axes can be found in figure 5 in Takei and Katz [2013]. To explain clearly the rotation that we are about to describe, we need to describe it with respect to an axis. For this, consider a hypothetical z -axis that points out of the page. The rotation matrix should map the grain coordinates to the cartesian coordinates. This corresponds to a rotation such that the x_g -axis coincides with the x -axis. It can be seen that this corresponds to a counterclockwise rotation around the z -axis. The anisotropy direction (the x_g -axis) is aligned at an angle of $\frac{\pi}{4}$ radians to the shear plane, so a counterclockwise of $\frac{\pi}{4}$ needs to be performed. A counterclockwise rotation is described by a rotation matrix

$$R = \begin{bmatrix} \cos(\Theta) & -\sin(\Theta) \\ \sin(\Theta) & \cos(\Theta) \end{bmatrix}. \quad (36)$$

We have $\Theta = \frac{\pi}{4}$.

2.5.2 Rotation matrix in 3D torsional flow

In 3D torsional flow the anisotropy direction is aligned at an angle of $\theta = \frac{\pi}{4}$ radian to the shear plane (the (x,y) -plane). Locally at length scales much smaller than the dimensional height H and dimensional radius L of the cylinder, torsional deformation looks much like simple shear deformation. At the length scale of the domain the anisotropy direction is position-dependent. It is parallel to the $(\psi - z)$ -plane. The anisotropy direction corresponds to the direction of maximum tensile stress in the base-state solution for constant porosity $\phi = 0.05$. The second grain axis y_g corresponds to the direction of minimum tensile stress (this is actually a compressive stress). It is also aligned in the $(\psi - z)$ -plane. The third grain coordinate axis z_g extends radially outwards from the cylinder and corresponds to the r -axis in cylindrical coordinates. A figure of this configuration is given in figure 5c in Takei and Katz [2013]. We will determine a position-dependent rotation matrix that rotates the grain coordinate axes to the cartesian axes. We will do this in two steps. First a counterclockwise rotation of $\frac{\pi}{4}$ around the z_g -axis (in cylindrical coordinates this is the r -axis) is performed. The x_g -axis is then rotated to coincide with the ψ -axis and the y_g -axis is rotated to coincide with the z -axis. This rotation corresponds to a rotation matrix

$$R_1 = \begin{bmatrix} 0 & 0 & 1 \\ \cos(\Theta) & -\sin(\Theta) & 0 \\ \sin(\Theta) & \cos(\Theta) & 0 \end{bmatrix}. \quad (37)$$

where the (x_g, y_g, z_g) -axes are rotated to the (r, ψ, z) -axes. Note that that a coordinate system corresponding to the (r, ψ, z) -axes does not represent the cylindrical coordinate system. Instead it is a coordinate system with straight axes that can only be locally defined. This is not a problem, because we are not interested in using grain coordinates to describe position. We only use grain coordinates to describe direction. We do have locally that the ψ -direction corresponds to the \mathbf{e}_ψ direction in the cylindrical coordinate system. For the cylindrical coordinate system we have

$$\mathbf{e}_r = \mathbf{e}_x \cos(\psi) + \mathbf{e}_y \sin(\psi) \quad (38a)$$

$$\mathbf{e}_\psi = -\mathbf{e}_x \sin(\psi) + \mathbf{e}_y \cos(\psi). \quad (38b)$$

We can invert this to find

$$\mathbf{e}_x = \mathbf{e}_r \cos(\psi) - \mathbf{e}_\psi \sin(\psi) \quad (39a)$$

$$\mathbf{e}_y = \mathbf{e}_r \sin(\psi) + \mathbf{e}_\psi \cos(\psi). \quad (39b)$$

It can be seen that to express the local (r, ψ, z) unit vectors in the cartesian unit vectors we need to multiply by the matrix

$$R_2 = \begin{bmatrix} \cos(\psi) & -\sin(\psi) & 0 \\ \sin(\psi) & \cos(\psi) & 0 \\ 0 & 0 & 1 \end{bmatrix}. \quad (40)$$

where $\psi = \text{atan2}(x, y)$. The following matrix will then express the unit vectors corresponding to the grain coordinate axes in terms of the cartesian unit vectors

$$R = R_1 R_2. \quad (41)$$

Note that we have not described a rotation of the coordinate system above. We have only described a way to express the unit vectors in the (position-dependent) grain coordinate system in terms of the cartesian unit vectors. We are not required to calculate all components of (41). It can be seen in (35) that only R_{11} , R_{21} and R_{31} are required. These are given by

$$R_{11} = -\sin(\psi) \cos(\Theta) \quad (42a)$$

$$R_{21} = \cos(\psi) \cos(\Theta) \quad (42b)$$

$$R_{31} = \sin(\Theta). \quad (42c)$$

It has been verified in Paraview that the vector (R_{11}, R_{21}, R_{31}) does indeed represent the anisotropy direction in the cartesian coordinate directions.

2.6 Complete dynamic anisotropy

Under dynamic anisotropy the anisotropy direction is the direction of maximum tensile stress. In order to determine this direction we need to determine the eigendecomposition of the stress tensor

$$\sigma_{ij} = D \Lambda D^T. \quad (43)$$

Here D is a matrix of eigenvectors and Λ is a diagonal matrix with eigenvalues on the diagonal. It does not matter for the computation of either the anisotropy direction or anisotropy magnitude whether we use the deviatoric stress tensor or the full stress tensor. We have that R_{11}, R_{21} and R_{31} are the components of eigenvector corresponding to the largest eigenvalue. From an implementational standpoint the stress tensor could be calculated in a way similar to the way the compaction rate is currently calculated in the code, using a very simple weak formulation. In this case it will be necessary to use tensor-valued test functions in the weak formulation. It has so far not been necessary to apply the full rotation matrix but it is perhaps worth pointing out that in Takei and Katz [2013] the second grain coordinate direction y_g corresponds to the direction of minimum tensile stress and z_g corresponds to the third remaining direction. The direction of the z_g -direction is similar to the way the cartesian coordinate system is defined, but then with (x_g, y_g, z_g) -axes.

2.7 Incomplete dynamic anisotropy

Under incomplete dynamic anisotropy the anisotropy direction is the direction of maximum tensile stress parallel to a fixed plane. The true direction of maximum tensile stress may have a component normal to this plane. The notion of incomplete dynamic anisotropy does not make any sense for 2D simple shear flow where there is only a single plane and we can consider either fixed anisotropy or dynamic anisotropy. For 3D torsional flow the fixed plane in which the anisotropy direction must lie is the (ψ, z) -plane. The numerical simulations in Katz and Takei [2013] have been performed for incomplete dynamic anisotropy. This is the reason that the notion is considered in this report. It is desirable to keep as many aspects of the simulation constant, and consider only the effect of the use of cartesian instead of cylindrical coordinates. Dynamic anisotropy in a fixed plane is expected to lead to large unphysical deviations for inclusion bead simulations that model the experiments Qi et al. [2013] Qi et al. [2014].

To enforce that the anisotropy direction is parallel to a fixed plane we first need to express the stress tensor σ_{ij} , which is given in the continuum cartesian coordinates, in continuum cylindrical coordinates. As mentioned earlier on the cartesian coordinate system cannot be transformed into the cylindrical coordinate system using a rotation. However, given x, y it is possible to express the $(\mathbf{e}_r, \mathbf{e}_\psi)$ directions in terms of the $(\mathbf{e}_x, \mathbf{e}_y)$ directions using a transformation that has the structure of a rotation matrix. It is described by

$$R = \begin{bmatrix} \cos(\psi) & \sin(\psi) & 0 \\ -\sin(\psi) & \cos(\psi) & 0 \\ 0 & 0 & 1 \\ , & & \end{bmatrix} \quad (44)$$

where $\psi = \text{atan2}(y, x)$ radians. The stress tensor in cylindrical coordinates is then

$$\tilde{\sigma} = R\sigma R^T. \quad (45)$$

$\tilde{\sigma}$ is the stress tensor in cylindrical coordinates and σ is the stress tensor in cartesian coordinates. The cylindrical coordinates are ordered (r, ψ, z) . Therefore the components of the stress tensor in the ψ - z plane are given by

$$\begin{bmatrix} \tilde{\sigma}_{\psi\psi} & \tilde{\sigma}_{\psi z} \\ \tilde{\sigma}_{\psi z} & \tilde{\sigma}_{zz} \end{bmatrix} = \begin{bmatrix} \tilde{\sigma}_{22} & \tilde{\sigma}_{23} \\ \tilde{\sigma}_{23} & \tilde{\sigma}_{33} \end{bmatrix} \quad (46)$$

We calculate the largest eigenvalue λ_1 and the smallest eigenvalue λ_2 , and the corresponding eigenvectors $\mathbf{v}_1, \mathbf{v}_2$ of this matrix. The rotation matrix that rotates from the cylindrical coordinates to the principal coordinates is then given by

$$R = \begin{bmatrix} \mathbf{0} & \mathbf{v}_1 & \mathbf{v}_2 \\ 1 & 0 & 0 \end{bmatrix} \quad (47)$$

The first principal coordinate corresponds to the direction of maximum tensile stress in the fixed plane. The second principal coordinate is the direction of minimum tensile stress in the fixed plane. The third principal coordinate is the direction normal to the fixed plane, where the geometric relation of z_g to x_g and y_g is the same as the geometric relation of z to x and y . The rotation matrix that expresses the unit vectors in the principal coordinates to the unit vectors in the cartesian coordinates is the product of the above two rotation matrices.

2.7.1 Magnitude of anisotropy for dynamic anisotropy

The anisotropy magnitude is given by

$$\alpha = 2 \tanh\left(\frac{2(\lambda_1 - \lambda_2)}{\sigma_{sat}}\right). \quad (48)$$

λ_1 is the maximum tensile stress and λ_2 is the minimum tensile stress, which will often be a compressive stress. It does not matter whether we calculate the anisotropy magnitude based on the deviatoric stress tensor or the full stress tensor. σ_{sat} is a material parameter. This parametrization of the anisotropy magnitude is given in Takei and Katz [2013].

2.8 Time-stepping under dynamic anisotropy

We have a system of equations for the liquid pressure p_f , compaction pressure p_c , solid velocity \mathbf{u}_s and porosity ϕ (23). As mentioned in section 2.2.2 we use a staggered scheme where alternately we solve the porosity-advection equation (23a) for the porosity, and the compaction equation (23b), modified bulk stress balance equation (23c) and the definition of the compaction pressure (23d). As mentioned before the use of a staggered scheme avoids having to solve a nonlinear system for the porosity. However under dynamic anisotropy the anisotropy magnitude and anisotropy direction are dependent on the stress field, which is a property of the solution. Solving simultaneously for the anisotropy magnitude, anisotropy direction and the other solution variables is very complicated. However this can easily be avoided by using the stress tensor from the previous time step. In Katz and Takei [2013] the same is done. As mentioned before from an implementational standpoint the stress can be calculated in the same way that the compaction rate is currently calculated in the code as a post-processing step.

2.9 A few notes on implementation of viscous anisotropy in FEniCS

As discussed in 2.5 and 2.4 the anisotropy term in the weak formulation in cartesian coordinates is given by

$$\frac{\dot{\epsilon}_{ij} + \dot{\epsilon}_{ji}}{2} \alpha \eta_\phi R_{i1} R_{j1} R_{k1} R_{l1} \dot{\epsilon}_{kl}. \quad (49)$$

One can see that there is a product of five position-dependent coefficients, the shear viscosity η_ϕ , and components of the anisotropy direction in cartesian coordinates R_{i1} , R_{j1} , R_{k1} and R_{l1} . Under dynamic anisotropy the anisotropy magnitude α is position-dependent too. In FEniCS the bilinear and linear forms of the weak formulation are described in so-called form files. The most simple way to implement this term in the form file is to write out this product of coefficients as it is presented here. It turns out that this gives wrong results. Examination of a form file with a product of two times the coefficient η_ϕ shows that the size of the compiled file is drastically smaller than when the terms contain at most one coefficient. This suggests that something wrong with the numerical integration of terms with products of coefficients. The conclusion is that FEniCS cannot handle products of coefficients. Depending on your point of view this is either an unavailable feature or a bug. FEniCS does not give a warning about it. An alternative way to implement this is to use a tensor-valued coefficient that is described in the main file. This is fourth-order tensor so it requires one to specify 81 components. In reality there are several symmetries. There is a feature that enables one to specify symmetries in tensors in FEniCS but it is not well documented. Perhaps implementing this symmetry will result in a code optimization. It is noted here that an alternative code where the entire contraction product was written out converged slightly slower. Another optimisation is to use an initial vector in the Krylov solver that resembles the base-state solution. This reduces the required number of iterations. We have also tried to express the conservation equations in terms of their perturbations from the base-state solution for isotropic viscosity, with a rescaling so that the perturbations are of order unity. This did not help. Implementing a condition that sets the mean pressure to zero did not help either, although we could only test this using standard preconditioner. As a final comment on the implementation we note that the development version of FEniCS reports an error that the element number is missing upon compilation of

the form files. It suggests that this is because vector elements are not supported in custom integrals. There is a thread about this on the FEniCS QA forum. However nobody has posted an answer yet.

3 Results

3.1 Validation of 2D Simple Shear Flow code

An important step in the process of developing a finite-element model is validation. Validation consists of verifying that the code does what it is intended to do and that it solves the right problem. In a finite element model this can be done by calculating a numerical solution for a given flow problem and comparing it to a known analytical solution. The codes for the 2D simple shear deformation problem and 3D torsional flow deformation problem make use of different viscosity tensors so we will validate the two codes separately. In this section we consider 2D simple shear flow. As mentioned in section (2.2.2) the finite element model that is developed in this project is intended for use in an alternating scheme. However it also makes sense to analyze it without considering the fact that it will ultimately be used in time-stepping. The model is concerned with solving compaction equation (23b), modified bulk stress balance (23c) and (23d) for the solid velocity \mathbf{u}_s , liquid pressure p_f and compaction pressure p_c for a given porosity ϕ . The advection equation is not solved. The boundary conditions in the paper that are used to calculate an analytical solution are given by

$$u_x = -1/2, \quad u_y = 0, \quad k_\phi = 0, \quad \text{at} \quad y = 0, \quad (50a)$$

$$u_x = 1/2, \quad u_y = 0, \quad k_\phi = 0, \quad \text{at} \quad y = 1. \quad (50b)$$

As mentioned in section 2.3 the code makes use of periodic boundary conditions at side boundaries $x = 0$ and $x = 1$. Also the weak formulation has been derived with the boundary condition $-k_\phi \nabla p_f \cdot \hat{\mathbf{n}} = 0$ at all boundaries. The simplest flow problem that we could consider for this domain and these boundary conditions consists of solving the compaction equation (23b), modified bulk stress balance (23c) and (23d) for a constant-porosity field. The numerical solution then reproduces the known base-state solution, namely simple shear deformation. However this flow problem is probably too simple to expose potential errors in the finite element model. A more complicated flow problem consists of simple shear deformation with a spatially-dependent porosity. This reflects more strongly the intended purpose of the code, the study of the growth of porosity perturbations. Porosity perturbations are, as the name implies, disturbances in the porosity field. It is known from experiments that these can grow and develop into coherently aligned high-porosity bands Spiegelman [2003]. The theoretical analysis of this pattern-forming instability is based on linearized analysis of sinusoidal perturbations

$$\phi_1 = \cos(K(\sin(\theta)x + \cos(\theta)y)) \quad (51)$$

to the base-state porosity ϕ_0 . Here θ is the angle at which the porosity perturbations are aligned to the shear plane and K is the angular wavenumber. The complete porosity field is given by

$$\phi = \phi_0 + \epsilon \phi_1. \quad (52)$$

Here ϵ is the amplitude of the porosity perturbations. An important assumption for the validity of linearized analysis is that the amplitude of the porosity perturbations is small. We choose a sufficiently small $\epsilon = 0.0001$. This results in a perturbation that has a much smaller magnitude than the base-state porosity ϕ_0 . Note that (51) and (52) specify the initial porosity perturbation that is used in the code. These expressions are not sufficient to perform linearized stability

analysis. In that case the entire time-dependent form of the solution must be specified. This includes a factor that models the growth of porosity perturbations and a factor that models the shearing of the porosity field by simple shear. These factors have been left out because they are relevant for a finite-element model. In linearized stability analysis the complete form is substituted into the conservation equations to solve for a parameter that controls the growth rate of porosity perturbations, the instantaneous growth rate \dot{s} . The instantaneous growth rate is computed for different angles of these sinusoidal perturbations in Takei and Katz [2013]. The angle with the maximum growth rate is expected to be the most visible in experiments, though high-angled bands will be quickly sheared away Spiegelman [2003]. In our validation we do not need to take this into consideration. We can only compute the instantaneous growth rate \dot{s} only at the initial time, because we do not solve the porosity advection equation (23a). Also, we only consider a single sinusoidal waveform.

The experiments show alignment of the porosity bands to the shear plane at angles of $\theta \approx \pi/9$. However the theory with an isotropic viscosity tensor predicts alignment at $\theta \approx \pi/4$. The theory of anisotropic viscosity has been developed to explain these lower angles. The use of a viscosity tensor leads to a growth rate curve as seen in figure 9(d) for saturated anisotropy $\alpha = 2.0$ in Takei and Katz [2013] and reproduced as the smooth curve in figure 3 in this report. Another parameter choice that has been used to compute this curve is $KR = 50.0$, where R is the nondimensional compaction length. This choice reflects the fact that the porosity perturbations have a much smaller wavelength than the length scale over which compaction pressures can be felt. We have spent some time trying to give a concise physical explanation for the shape of this curve, but this is surprisingly difficult, owing to a coupling under viscous anisotropy between the enhanced matrix shear due to spatially-dependent porosity (described in Spiegelman [2003]) and the growth of porosity perturbations. It is expected that reproducing this growth rate is a suitable validation of the 2D simple shear flow code. The instantaneous growth rate can be calculated using equation (5.16) in Takei and Katz [2013]

$$\dot{s} = -C_0 + (1 - \phi_0)\phi_1^{-1}C_1. \quad (53)$$

Here C_0 is the zeroth-order compaction rate and C_1 is the first-order compaction rate. It is known from theory that there is no base-state segregation in simple shear deformation under viscous anisotropy Takei and Katz [2013]. We can then compute $C_1 = \nabla \cdot \mathbf{u}_s$ based on the definition of the compaction pressure (23d). It is then found that

$$(1 - \phi_0) * \epsilon^{-1}/\zeta^{-1}. \quad (54)$$

An alternative method to calculate the compaction rate is to apply the FEM method to the equation

$$C_1 = \nabla \cdot \mathbf{u}_s. \quad (55)$$

The weak formulation is given by

$$\int_{\Omega} C_1 v \, dx = \int_{\Omega} \nabla \cdot \mathbf{u}_s v \, dx, \quad (56)$$

where v is an arbitrary test function. Calculating the compaction rate in this way gives results that are approximately the same. The numerical values are based on truncating the grid to cover the middle of the domain and examining the outermost extent of the scaling in Paraview, which should give the maximum and minimum growth rates measured in the region. The results based on the compaction pressure and the results based on the weak formulation for the definition of the compaction rate differ by at most e-2. For reproducibility the table 3.2 gives the coefficients that have been used in the simulation. A mesh size of 1000×1000 is used. We calculate the instantaneous growth rate at intervals of $\pi/12$. We next need to choose a suitable perturbation

variable	value
r_ζ	$\frac{5}{3}$
K	different values for different perturbation angles θ
θ	varies
λ	27.0
R	related to K
α	2.0
ϵ	0.0001
ϕ_0	0.05

Figure 1: coefficients used in the validation. λ is the coefficient of the shear viscosity, r_{rzeta} is the bulk/shear viscosity ratio.

wavelength for the porosity perturbation. It is important for the proper application of periodic boundary conditions that the porosity for a given y at the left boundary matches the porosity value at the right side of the domain for that y . For the following choice of the perturbation wavelength this is the case

$$\lambda = .25\sin(\theta). \quad (57)$$

This corresponds to about 8 complete waves in the domain for $\theta = \pi/12$. It is discussed in Katz and Takei [2013] that about 15 grid points are required to sufficiently resolve a single complete oscillation of the porosity perturbation, though the value of the instantaneous growth rate \dot{s} does differ a little from the analytical solution then. The mesh size that has been chosen should be sufficient to resolve the porosity perturbation. For very steep-angled bands the wavelength computed using (57) becomes too small as $\theta \rightarrow \pi/2$. Therefore a wavelength of $\lambda = .05\sin(\theta)$ is chosen for the simulations with $\theta = 5\pi/12$ and $\theta = 7\pi/12$. We have earlier made the assumption that $R = 50/K$. We can calculate that $R \approx 2.1$ for the choices we have made. This means that the influence of the boundary conditions can be felt throughout the domain according to the interpretation of the compaction length as the length scale over which the compaction rate can be felt. The direct solver MUMPS is used to solve the linear system resulting from discretization. The use of a direct solver makes sure that the solution of the linear system is solved exactly. This is important because it eliminates one possible source of error and we are interested in validating the implementation of the viscous anisotropy, not the solution techniques used to solve the linear system that results from discretisation of the weak formulation. In figure 2 the compaction pressure is shown for $\theta = \pi/12$, as an example of how the solution looks like. The perturbation growth rate curve is shown in figure 3. The deviation from the curve that represents the analytical solution can be almost wholly explained by the fact that the wavelength is sometimes too large, so that the profile is not sufficiently periodic. What could in theory also give a small difference is the fact that the bulk viscosity is defined as $(r_\zeta(\phi/p\eta_0)^{-1})$ in the code, instead of $\zeta_\phi = r_\zeta\eta_\phi$ and an exponential profile for the shear viscosity as in Takei and Katz [2013]. As mentioned in the introduction of this section the goal of validation is to ensure that the finite element model is working correctly and solving the right problem. In hindsight the above tests were not sufficient to establish this. It will turn out that for anisotropy magnitudes of around $\alpha \gtrsim \frac{4}{3}$ the velocity block in the assembled matrix (see section 3.4) loses the property of positive definiteness. The direct mumps solver can still solve the matrix for $\alpha = 2.00$. However it does lead to problems with convergence of the iterative solver. Also there will be a value of α for which the linear system of equations resulting from discretisation of the weak formulation is not invertible (aside from the fact that the pressure is defined up to a constant). This is unacceptable, because under dynamic anisotropy there will be a range of anisotropy magnitudes α throughout the domain.

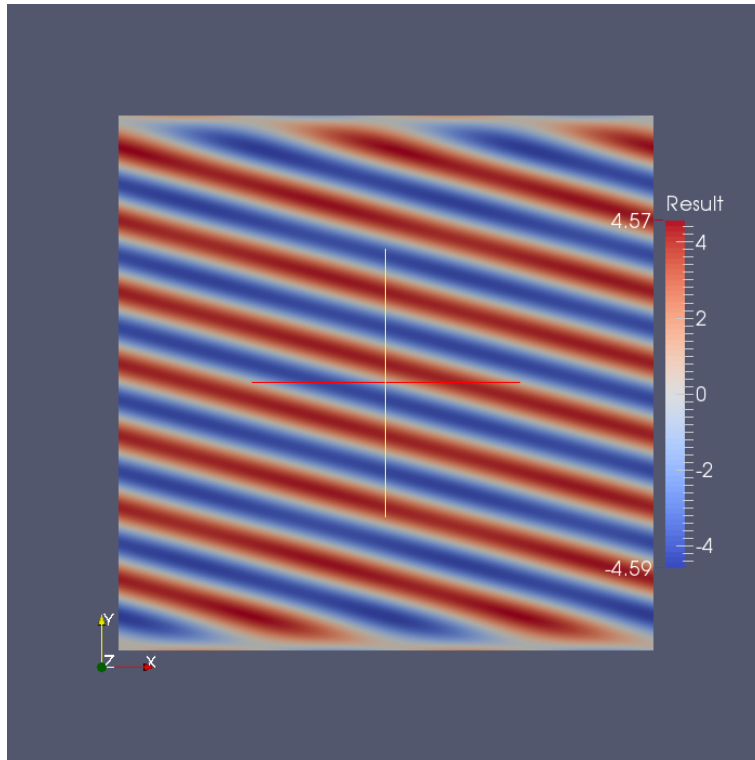


Figure 2: the high porosity band is here aligned at an angle of 15 degrees to the shear plane.

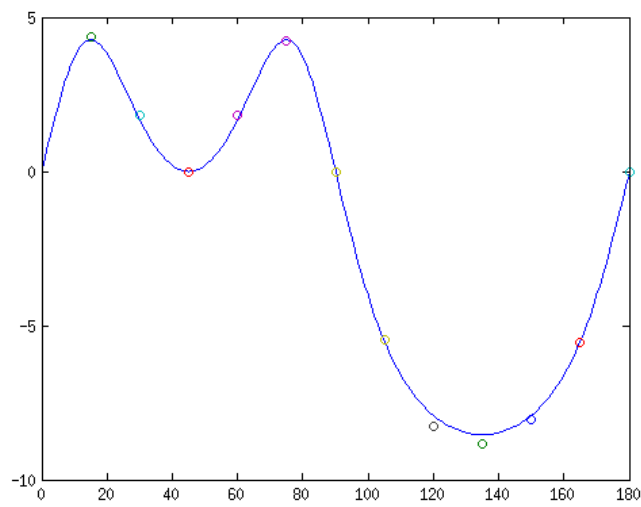


Figure 3: growth rate profile.

3.2 Convergence of the preconditioned iterative solver for the 2D simple shear slow case with anisotropy

In section 3.1 the direct mumps solver is used to solve the linear system resulting from discretisation of the weak formulation. Unfortunately direct solvers use too much memory for very large 3D simulations, as in torsional flow. Therefore iterative solvers are used. As a test, it is applied to 2D simple shear. One way to accelerate the performance of iterative solvers is by use of a preconditioner. In section 3.4 preconditioners are explained. In Rhebergen et al. [2014] a preconditioner is introduced for the three-field equations for coupled mantle/magma dynamics. In this section this preconditioner is applied without any modification for viscous anisotropy to the compaction equation (23b), modified bulk stress balance (23c) and (23d) for a constant-porosity field. The reason that the velocity block K (see section 3.4) has not been modified is that it turns out that it becomes indefinite if you add an anisotropy term. Note that in this section the term velocity block K can refer both to the velocity block in the preconditioner and the matrix resulting from discretisation of the conservation equations depending on the context. The fact that the velocity block K becomes indefinite means that the multigrid algorithm used in the preconditioner cannot invert it well. If a small mesh size is used and LU-factorization is used to invert the velocity block K a performance improvement is gained, but the preconditioner still does not work to satisfaction because of a considerable dependence of the performance on the anisotropy magnitude α and the mesh size h . We also note here that not using any preconditioner at all or using a standard preconditioner from numerical linear algebra results in poor performance. In this section results are instead given for a preconditioner that has not been modified for viscous anisotropy. The performance is expected to decrease because in comparison to the isotropic case because the velocity block (see section 3.4) in the preconditioner resembles the actual velocity block in the discretisation of the weak formulation less well. All simulations have been run with a maximum of a million iterations. We have used the following values for the parameters. The bulk/shear viscosity ratio is given by $r_\zeta = 5.0/3.0$, the coefficient for the porosity-dependence of the shear viscosity is given by $\lambda = 27.0$, the nondimensional compaction length is given by $R = 1.0$. The GMRES iterative solver is applied with a restart value of 300. Testing indicates that GMRES works better than BiCGstab. Aside from this parameters of the linear solver are left unchanged from the existing code. All modifications of the parameters that we have tested so far result in worse performance. The results of the simulations are shown in table 3.2. A very large number of

mesh size	BC type	number of iterations	order of residual in 1000000 iterations	α
100	periodic	7705	e-8	2.0
100	dirichlet	n.a.	e-7	2.0
30	periodic	15	e-15	0.0
30	periodic	16	e-15	.5
30	periodic	19	e-15	1.
30	periodic	37	e-15	1.5
30	periodic	709	e-15	1.6
30	periodic	313090	e-9	1.7
30	periodic	5072	e-16	1.8
30	periodic	7731	e-16	1.9
30	periodic	2901	e-16	2.0

Figure 4: simulation results for the standard three-field preconditioned iterative solver.

iterations is required for $\alpha = 1.7$. This might be related to loss of positive definiteness in the velocity block of the discretisation of the weak formulation. It can be seen that this also has

implications for the condition number of the problem of inverting the linear system. As the anisotropy magnitude α is varied, the eigenvalues of the velocity block K vary continuously. A symmetric real matrix is positive definite if and only if it has positive eigenvalues. In order for the velocity block K to become indefinite, it must have zero eigenvalues at some anisotropy magnitude α , which means that it is not invertible there. It should be noted that this is a problem of the three-field formulation of the conservation equations, it is not a problem related to the solution method. As mentioned it is possible that the velocity block K becomes singular at some point and that this causes the very large number of iterations required, and the high relative residual achieved, at $\alpha = 1.7$. That said, there is a problem with this hypothesis. It has been verified using an implementation of viscous anisotropy into a Python code for coupled magma/mantle dynamics, and Matlab, that the matrix K becomes indefinite for a mesh size of 10×10 at an anisotropy magnitude of $\alpha \approx 1.37$. This is close to the value $\alpha = \frac{4}{3}$ predicted by an analysis of the modified bulk stress balance equation in grain coordinates. Perhaps the difference can be explained by the small mesh that is used and the influence of the periodic boundary conditions on the eigenvalue structure of the velocity block K . $\alpha = 1.7$ is a long way off from $\alpha \approx 1.38$ however, so it is questionable whether this is a good explanation of the aberrance of the simulation results for $\alpha = 1.7$.

At high anisotropy magnitudes $\alpha \geq 1.8$ it can be seen that the required number of iterations is fairly large, but there is convergence. We expect that this is a result of the fact that the velocity block K used in the preconditioner and the velocity block K in the discretisation of the weak formulation of the three-field equations have a different structure.

We have made one other observation that indicates that the results for $\alpha = 1.7$ are problematic. This observation has also been made for $\alpha = 1.6$, which does seem to converge. In these simulations the relative residual norm often seems to be increasing rather than decreasing. This is not prohibited by the fact that we are using restarted GMRES. During each restart, restarted GMRES will minimize the preconditioned residual norm. We do not know how to explain this, except for pointing out that it may be related to the loss of positive definiteness of the velocity block K as discussed above.

The results for simulations 2 and 3 show that the choice of boundary conditions has implications for the convergence of the iterative solver. The iterative solver converges to the order $e - 8$ when Dirichlet boundary conditions are applied on the top and bottom wall and periodic boundary conditions are applied on the side walls. When the Dirichlet boundary conditions are applied at all walls it converges to $e - 7$. The analytical solution is the same for either choice of boundary condition. Of course for the porosity-dependent case the Dirichlet boundary conditions at the side boundaries will create an additional disturbance, because the Dirichlet BC will prohibit movement of the solidout of the melt-bands at the BC. These simulations suggest that the choice of boundary conditions may also have implications for the convergence in the 3D torsional flow case. Here we also have that for the porosity-dependent case the Dirichlet boundary conditions at the outer edge will prohibit flow of the solidout of the melt-bands. Here the convergence of the iterative solver may be reduced in the constant-porosity case, even though the analytical solutions match for the two boundary conditions.

Other simulations suggest that this may be a phenomenon related to the use of the three-field formulation. We will now examine simulation results for the two-field formulation of 2D simple shear flow. This formulation is considered because the velocity block K becomes indefinite for \gtrsim in the three-field formulation of 2D simple shear flow. A theoretical motivation for using a two-field formulation is given in the following. It is known from numerical analysis that positive definiteness of a matrix that is the result of discretisation of the weak formulation is related to ellipticity of the underlying equations. A second-order partial differential equation is elliptic if all the coefficients of the second-order terms are positive. Examination of the modified bulk stress balance equation in grain coordinates (23c) shows that the coefficient of

the elongation rate in the direction of anisotropy term $\frac{\partial^2 u_{x_g}^s}{\partial x_g^2}$ where x_g is the anisotropy direction is given by

$$\frac{4}{3} - \alpha. \quad (58)$$

It follows from this that in grain coordinates ellipticity is lost for $\alpha \geq 4/3$. It is a question to what extent this result can be extended to 2D simple shear flow in cartesian coordinates and 3D torsional flow in cartesian coordinates. In 2D simple shear flow the anisotropy direction and the anisotropy magnitude are constant. This suggests that the result that ellipticity is lost for $\alpha \geq 4/3$ may be meaningful even in cartesian coordinates. On the other hand if the modified bulk stress balance equation is examined in cartesian coordinates then the anisotropy term $\alpha \eta_\phi \delta_{i1} \delta_{j1} \delta_{k1} \delta_{l1} \dot{e}_{kl}$ is replaced by $\alpha \eta_\phi R_{i1} R_{j1} R_{k1} R_{l1} \dot{e}_{kl}$. The anisotropy term now gives a smaller contribution to the coefficients of individual second order terms in the modified bulk stress balance. A further examination is required to see if any coefficients become negative, and whether ellipticity can depend on the coordinate system at all. The same goes for 3D torsional flow. It was mentioned before that ellipticity of systems of equations is related to positive definiteness of the matrix resulting from their discretisation. We have verified that in the three-field formulation the velocity block K becomes indefinite for $\alpha \approx 1.37$ in a 2D simple shear problem with constant porosity, a mesh size of 10×10 and periodic boundary conditions at the side wall. We have also determined that a 3D torsional flow problem with $N = 5$, corresponding to 5 elements between the axis of the cylinder and its outer edge, the velocity block K remain positive definite up to $\alpha = 2.00$. The reason we have performed simulations with the two-field preconditioner is that it can be easily seen by examination of the modified bulk stress balance in grain coordinates that the coefficient of the elongation rate in the direction of anisotropy term $\frac{\partial^2 u_{x_g}^s}{\partial x_g^2}$ is positive for all physical values of the anisotropy magnitude α . This suggests the problems considered in the above section may be absent in the two-field formulation of the conservation equations. Because the velocity block K now remains positive definite it can be (approximately) inverted by the multigrid algorithm. This enables us to modify the preconditioner by adding the same anisotropy term as in the weak formulation of the conservation equations. This is expected to improve performance in comparison to the standard preconditioner. The iterative solver BiCGstab is used. In table 3.2 results are given for simulations.

mesh size	BC type	number of iterations	order of residual	α
100	periodic	35	e-15	2.0
100	Dirichlet	33	e-15	2.0
100	periodic	25	e-15	0.0
30	periodic	20	e-15	2.0
30	periodic	15	e-15	0.0

Figure 5: simulation results for the standard three-field preconditioned iterative solver.

It can be seen that the boundary condition only has a small effect on convergence. Also, the performance of the preconditioner has a relatively small dependence on the anisotropy magnitude α and the mesh size h . It was discussed in the introduction of this section that modifying the preconditioner by adding the anisotropy term is possible in the three-field case if we use the direct LU-solver to invert the resulting velocity block K . However the required number of iterations for convergence is then still much larger than seen in this table, indicating that the bad convergence in the tests with the standard preconditioner was not only a result of a preconditioner unmodified for anisotropy but also an inappropriate formulation of the physical problem.

In conclusion the applying the standard preconditioner to the three-field formulation results in poor performance. Applying the modified preconditioner to the two-field formulation results in good performance.

3.3 Condition number of the 2D Simple Shear Flow case

We have made the observation that, even though using the preconditioner gives an improvement over not using the preconditioner in the three-field formulation, the required number of iterations increases drastically as the anisotropy magnitude increases. Also in the 3D Torsional Flow case perturbations appear for high anisotropy magnitude. Either of these observations indicate that the problem might become ill-conditioned for high anisotropy magnitude. This is intuitively plausible. As the anisotropy magnitude approaches 2.0 a kind of limit behaviour occurs. The 2D Simple Shear Flow and 3D Torsional Flow case will then both have a fluid where the elongation rate in the anisotropy direction does not contribute to the tensile stress in the anisotropy direction independent of the volumetric strain. One can see this as follows for the 2D Simple Shear Flow case. Consider the incomplete constitutive equation for the bulk stress tensor 4

$$\sigma_{ij} = -p_f \delta_{ij} + C_{ijkl} \dot{e}_{kl}. \quad (59)$$

The volume fraction of the solid $1 - \phi$ has been neglected here. We are here concerned with the deviatoric stress tensor

$$\sigma_{ij} = C_{ijkl} \dot{e}_{kl}. \quad (60)$$

Write out this contraction product in grain coordinates for the component of the stress tensor that represents the normal stress in the anisotropy direction.

$$\sigma_{\sigma_3 \sigma_3} = C_{\sigma_3 \sigma_3 \sigma_3 \sigma_3} e_{\sigma_3 \sigma_3} + 2C_{\sigma_3 \sigma_3 \sigma_1 \sigma_3} e_{\sigma_1 \sigma_3} + C_{\sigma_3 \sigma_3 \sigma_1 \sigma_1} e_{\sigma_1 \sigma_1}. \quad (61)$$

The viscosity tensor in grain coordinates is given by

$$C_{ijkl} = \zeta \delta_{ij} \delta_{kl} + \eta (\delta_{ik} \delta_{jl} + \delta_{il} \delta_{jk} - 2/3 \delta_{ij} \delta_{kl}) - \Delta \delta_{ix_g} \delta_{jx_g} \delta_{kx_g} \delta_{lx_g}. \quad (62)$$

Here we will use the definition of the shear viscosity that is used in Takei and Katz [2013], not the redefinition that is used in the code. Also I will use the constitutive equations from ? set. We now find components

$$C_{\sigma_3 \sigma_3 \sigma_3 \sigma_3} = \zeta + 4/3 \eta - \Delta = 5/3 \eta + 4/3 \eta - \alpha \eta = (3 - \alpha) \eta, \quad (63a)$$

$$C_{\sigma_3 \sigma_3 \sigma_1 \sigma_3} = 0, \quad (63b)$$

$$C_{\sigma_3 \sigma_3 \sigma_1 \sigma_1} = \eta. \quad (63c)$$

We then find that

$$\sigma_{\sigma_3 \sigma_3} = (3 - \alpha) \eta e_{\sigma_3 \sigma_3} + \eta e_{\sigma_1 \sigma_1}. \quad (64)$$

Now consider the case of saturated anisotropy $\alpha = 2.00$. We then find

$$\sigma_{\sigma_3 \sigma_3} = \eta e_{\sigma_3 \sigma_3} + \eta e_{\sigma_1 \sigma_1} = \eta e_v = 0. \quad (65)$$

The last follows from the absence of volumetric strain in simple shear flow, which is the solution even for anisotropic viscosity when the porosity is constant. It is hypothesized that this absence of tensile shear stress in the direction of anisotropy has a negative effect on the condition number of the discretisation of the weak formulation of the conservation equations. The condition number is seen as a measure for how hard it is to solve a problem. To verify or falsify this hypothesis we compute the condition number for mesh sizes 10×10 , 20×20 , 30×30 . Looking back on this section we recognize that the relevance of the results in this section is dubious.

The hypothesis was that a property of the bulk stress tensor under viscous anisotropy might make it hard to solve the conservation equations. However we are not actually solving a bulk stress balance equations where the tensile stress in the anisotropy direction appears as it is given above. Instead, in the three-field formulation, a modified bulk stress balance equation is solved where bulk viscosity does not appear in the relation between the tensile stress in the anisotropy direction and the elongation rate in the anisotropy direction (note that we are now using physical terms to describe the mathematical formulation of the problem). This means that at $\alpha = 2.0$ there is nothing special about the relationship between the elongation rate in the anisotropy direction and the tensile stress in the anisotropy direction. The elongation rate in the anisotropy direction in the anisotropy direction influences the tensile stress in the anisotropy direction both through the volumetric strain contribution and a contribution of its own. This means that there is no reason to believe that the problem may become ill-conditioned at saturated anisotropy. In principle we may use any formulation we want to solve the physical problem but the three-field formulation has its own problems in that the velocity block is expected to become indefinite at anisotropy magnitude $\alpha = \frac{4}{3}$. We will let this section remain in the report for later reference. The condition number can be calculated as

$$\text{condition number} = \frac{\text{largest singular value}}{\text{smallest singular value}}. \quad (66)$$

The singular values can be computed by applying the singular value decomposition to the matrix that results from discretization of the weak formulation. A problem that occurs here is that the matrix is actually singular because the pressure is only determined up to a constant. This means that we cannot determine the condition number. A first workaround is to examine the second smallest magnitude singular value and to calculate a proxy for the condition number based on this. This is easy, but it is not known to us whether the usual interpretation of the condition number in terms of the accuracy to which we can calculate the solution still applies. We will first examine the influence of the mesh size on the proxy of the condition in a flow case without anisotropy $\alpha = 0.0$. The results are given in table 3.3. An increase in the condition

mesh size	largest singular value	second smallest singular value	proxy for the condition number
10	6.08e-4	1.42e+1	2.32e+5
20	1.52e-4	1.42e+1	9.34e+5
30	6.76e-5	1.42e+1	2.10e+6

Figure 6: singular values and proxy for the condition number in the three-field formulation of 2D simple shear flow.

number as the mesh size increases is to be expected, see Brenner and Scott [2008]. Let us now examine the effect that anisotropy has on the condition number. We take a mesh of size 10×10 . There is no indication here that the velocity block K becomes ill-conditioned for high anisotropy magnitude α . It is known from experiments using an implementation of viscous anisotropy in a Python code for coupled magma/mantle dynamics, and Matlab, that the velocity block K becomes indefinite at an anisotropy magnitude $\alpha \approx 1.37$. No anisotropy magnitudes close to this values are shown in table 3.3. It is known from experimentation that only anisotropy magnitudes very close to the value where the velocity block K is singular, which by theory we know must exist, result in smallest singular values that are significantly smaller than in this table.

A more rigorous approach for establishing a condition number for the problem of solving the conservation equations is to define an absolute pressure. The simplest approach would be to set the value of the pressure at one of the grid points. This is described on p.391 of Logg et al. [2012]. However nothing seems to happen when we implement this method, and this problem

anisotropy	largest singular value	second smallest singular value	proxy for the condition number
0.5	6.22e-4	1.42e+1	2.28e+5
1.0	6.46e-4	1.42e+1	2.19e+5
1.5	7.07e-4	1.42e+1	2.00e+5
1.6	5.00e-4	1.42e+1	2.83e+5
1.7	7.28e-5	1.42e+1	1.95e+6
1.8	1.61e-4	1.42e+1	8.79e+5
1.9	6.60e-5	1.42e+1	2.15e+6
2.0	1.83e-4	1.42e+1	7.74e+5

Figure 7: the anisotropy number for different values of the anisotropy magnitude.

is reported by others as well on the FEniCS board. An alternative is to require that the mean pressure is zero

$$\int_{\Omega} p_f dx = 0. \quad (67)$$

This condition can be applied by using an additional Lagrange multiplier

$$\int_{\Omega} cq dx + \int_{\Omega} p_f d dx \quad (68)$$

in the weak formulation as described in the demo for the Poisson equation with pure Neumann boundary conditions in the FEniCS documentation. Here c is a new trial function, q is the test function corresponding to the liquid pressure, p is the liquid pressure, d is a new test function. It does not matter for the solution whether you add or subtract these terms. The results are described in the table Again the problem is expected to become singular for anisotropy

anisotropy	largest singular value	minimum singular value	condition number
0.0	1.01e-06	1.416350374175e+01	1.399301697500e+07
.5	1.01e-6	1.42e+1	1.40e+07
1.0	1.01e-6	1.42e+1	1.40e+07
1.5	1.01e-6	1.42e+1	1.40e+07
2.0	1.01e-6	1.42e+1	1.40e+07

Figure 8: condition numbers for the three-field 2D simple shear flow problem with a condition on the mean pressure.

magnitudes close to $\alpha = 1.37$, but no anisotropy values close to this value were considered.

In conclusion the condition number does not seem to vary much for most values of the anisotropy magnitude α . However this is illusory because for $\alpha \approx 1.37$ the matrix resulting from discretisation of the three-field conservation equations becomes singular. For anisotropy values larger than this the velocity component becomes indefinite which will prevent the preconditioner from working well. Also, the 3D torsional flow problem is similar over small length scales to 2D simple shear flow. Tests indicate that the numerical perturbations in three-field 3D torsional flow disappear in the two-field formulation. This constitutes an additional problem of the three-field formulation.

3.4 Eigenvalues of the velocity component of the assembled matrix

As mentioned earlier on FEniCS is a finite element assembler. Assembly refers to the discretisation of the weak formulation of the conservation equations. This results in a linear system of equations. In principle FEniCS automates this for us. However it is helpful to consider the

structure of the matrix that is assembled in order to examine what goes wrong in the modified preconditioner for the three-field formulation when anisotropy is implemented. After assembly the matrix has the following structure

$$A = \begin{bmatrix} K_\eta & G^T & G^T \\ G & -C_k & 0 \\ G & 0 & -Q_\zeta \end{bmatrix}. \quad (69)$$

Here K_η is the discretization of the bilinear form

$$\int_{\Omega} \eta_\phi \mathbf{D}\mathbf{u}_s : \mathbf{D}\mathbf{v} \, dx + \int_{\Omega} (\zeta_\phi - \frac{1}{3}\eta_\phi)(\nabla \cdot \mathbf{u}_s)(\nabla \cdot \mathbf{v}) \, dx - \int_{\Omega} \frac{\dot{e}_{ij} + \dot{e}_{ji}}{2} \alpha \eta_\phi R_{i1} R_{j1} R_{k1} R_{l1} \dot{e}_{kl} \, dx. \quad (70)$$

G is the matrix that results from discretisation of

$$- \int_{\Omega} p_f \nabla \cdot \mathbf{v} \, dx. \quad (71)$$

C_k is the matrix that results from discretisation of

$$\int_{\Omega} k_\phi \nabla p_f \cdot \nabla q \, dx. \quad (72)$$

Q_ζ is the matrix that results from discretization of

$$\int_{\Omega} \zeta_\phi^{-1} p \omega \, dx. \quad (73)$$

It can be seen that the only change that results from the implementation of viscous anisotropy is that the velocity component K_η has changed. Therefore we will re-examine assumptions in Rhebergen et al. [2014] that relate to K . It is important for the theory in the preconditioner paper that the shear viscosity can be separated from the velocity component

$$K_\eta = \eta K. \quad (74)$$

This is clearly still the case when anisotropy is implemented. It is also important that K stays symmetric. We have tested that this is the case. For the other assumptions that we want to verify it is better to first consider what preconditioning is. A preconditioner works as follows. Suppose that we are solving a linear system

$$Ax = b. \quad (75)$$

In this case (A, b) corresponds to the linear system that is the result of discretisation of the weak formulation. The convergence of iterative methods for linear systems is often slow. It turns out that convergence is faster for systems with eigenvalues that are close to each other. This idea can be exploited to construct a preconditioner. We multiply the system by a matrix P^{-1} where P resembles A in some sense

$$P \approx A. \quad (76)$$

but where we also have that P^{-1} is cheap to calculate. The iterative solver should then converge better for the system

$$P^{-1}Ax = P^{-1}b, \quad (77)$$

because the eigenvalues are closer together. x is still the solution of the original system. The preconditioner paper makes a distinction between a theoretical preconditioner and a practical preconditioner. The theoretical preconditioner is defined as

$$A = \begin{bmatrix} \eta K & 0 & 0 \\ G & R & 0 \\ G & T & S \end{bmatrix}. \quad (78)$$

Here R , S and T are functions of $GK^{-1}G$. It is possible that the spectrum of the preconditioned matrix will be broader as a result of the implementation of anisotropy. As a proxy for this, I will first determine the eigenvalues of the matrix K . For a symmetric real positive definite matrix, the singular values and eigenvalues coincide. However testing using an implementation of viscous anisotropy in a code using the Python version of FEniCS and Matlab indicates that the positive definiteness of K is lost between 1.30 and 1.40. The precise value seems to depend on the mesh size and whether the periodic BCs are used at the side boundaries. It is also possible to use Dirichlet boundary conditions at the sides. From a physical point of view the system of conservation equations is not expected to become singular at any value of the anisotropy magnitude. This is a problem of the three-field formulation of the conservation equations, as described at the end of section 3.2. The velocity block K for the two-field formulation is positive definite for all physical anisotropy values.

As a final remark on the preconditioner for the three-field formulation we mention that theorem 4.2 in Rhebergen et al. [2014] still applies. The generalized eigenproblem with the theoretical preconditioner on the right hand side has eigenvalues 1, σ , both when $\alpha = 0.0$ and $\alpha = 2.0$. In other words the theoretical preconditioner should work for the three-field preconditioner, except for the anisotropy values close to $\alpha \approx 1.37$ where the velocity block K is singular. Since the latter is unacceptable this is a result of little relevance.

3.5 Validation of the 3D Torsional Flow case without anisotropy

As mentioned the purpose of validation is to ensure that a finite-element model works as intended and that it solves the right problem. A simple test for the three-field finite-element model for torsional deformation is to reproduce the base-state compaction profile under anisotropy for a constant porosity field. In order to prevent confusion we point out that these are results that are valid instantaneously at the initial time. The finite-element model is intended for use in a code that also involves time-stepping, but no time-stepping has been performed in this project. A glance at the results in figures 9 and 10 shows that the three-field finite-element model for torsional flow does not work well. All figures of torsional simulations in this reported have been computed with the direct mumps solver. Therefore the perturbations cannot be a result of a poor solution of the linear system. The results suffer from unphysical perturbations. We have concluded that these perturbations are the result of numerical instability. Arguments for this conclusion will be given in the following sections. One reason that we will give here is that the base-state compaction profile reproduces most of the features from the analytical results in figure 6(b) in Takei and Katz [2013]. The compaction rate at the side wall of the cylinder is approximately the same, the direction of base-state segregation is the same and the radius at which the compaction rate is zero is approximately the same. There is a deviation at the axis of the cylinder. This is understood to be a result of the fact that the anisotropy direction is ill-resolved there under fixed anisotropy. The small numerical differences elsewhere in the domain may be a result of the small mesh size and the fact that a secondary flow develops due to the truncation of the cylinder. This secondary flow is described in section 13. A picture is not included but it can be seen that the perturbations are somewhat aligned in the plane

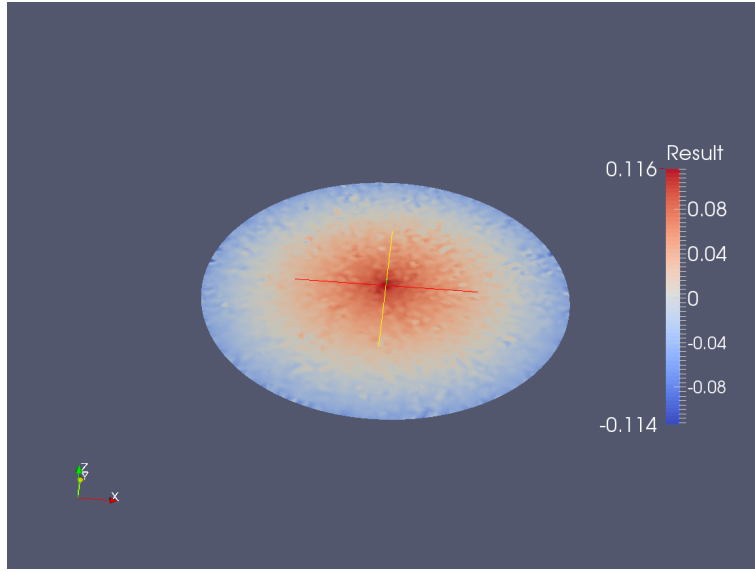


Figure 9: compaction rate in the $z=1/2$ plane for nondimensional compaction length $R = 1$. The number of elements from the axis of the cylinder to the outer edge is $N = 30$. It can be seen that there are perturbations overlying a smooth base-state compaction profile.

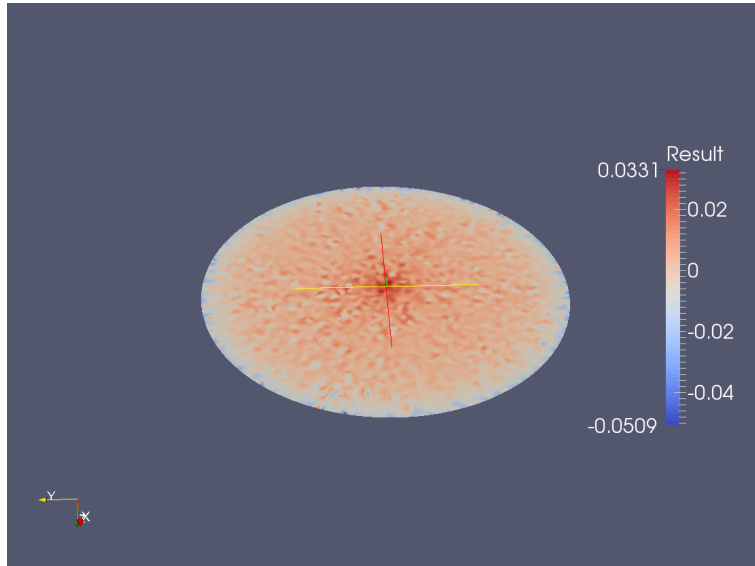


Figure 10: compaction rate in the $z=1/2$ plane for nondimensional compaction length $R = 0.1$. The number of elements from the axis of the cylinder to the outer edge is $N = 30$. It can be seen that there are perturbations overlying a smooth base-state compaction profile.

normal to the anisotropy direction. This is suggestive in the light of the fact that the coefficient in front of the elongation rate in the anisotropy direction $\frac{\delta^2 u_g}{\delta x_g^2}$ is negative for $\alpha > 4/3$. These are all the features of three-field simulations of base-state compaction that we would like to show.

The two-field finite element model for 3D torsional flow does not give any perturbations in a simulation of base-state compaction, though a figure is not included. This is one of the reasons to conclude that the perturbations in the three-field formulation are the result of a numerical instability. In principle the smooth profile of the base-state compaction should enable one to perform a formal validation of the two-field formulation for torsional deformation. Such a validation consists of calculating the perturbation growth rate profile for saturated anisotropy $\alpha = 2.0$. The growth rate of porosity perturbations can be calculated as

$$\dot{s} = -C_0 + (1 - \phi_0)\epsilon^{-1}C_1. \quad (79)$$

Here C_0 is the base-state compaction rate and C_1 is the first order compaction rate. $\epsilon = 0.0001$ has been chosen so that the assumptions of linearized stability analysis are still valid. The volumetric strain rate cannot be immediately decomposed into base-state C_0 and first-order C_1 components. However one could first perform a constant porosity simulation where C_0 is calculated and a second simulation with a spiral-staircase shaped porosity field where C_1 is calculated by subtracting C_0 from C_1 . We do not have sufficient time to perform this validation but it would be desirable to perform it as additional confirmation that the implementation of viscous anisotropy is correct from a physical standpoint.

As mentioned the perturbations are not present in the two-field formulation of 3D torsional flow. This was an unexpected result because the velocity component K does not lose positive definiteness in the 3D torsional flow problem. As mentioned it has been determined that the modified conservation equations in grain coordinates lose the property of ellipticity for $\alpha \geq 4/3$. However we whether we can extend this conclusion to torsional deformation. The anisotropy direction is dependent on position in torsional deformation and the individual components of the viscosity tensor become smaller, when cartesian coordinates are used. It may be worthwhile to examine in more detail whether the modified conservation equations are elliptic in the torsional case. If the conservation equations remain elliptic then there must be another problem causing the numerical instability in the three-field formulation of torsional flow. In general we can say that Stokes flow seems to be sensitive to numerical instability. In particular there is a property of inf-sup instability that has been proven in the numerical analysis literature for P2-P1 elements but not it has not been proven in Rhebergen et al. [2014] for P2-P1-P1 elements. This was not necessary for the finite-element model for coupled magma/mantle dynamics because instability does not occur in the absence of viscous anisotropy. It might be worthwhile to examine inf-sup stability using analytical arguments. We do note here that perturbations do not occur in the three-field formulation of simple shear deformation, but this might be the result of the absence of several features of the domain and viscosity tensor in torsional deformation that are discussed in later sections.

As mentioned the perturbations in the three-field formulation prevent a good validation. However the perturbations are absent when there is no viscous anisotropy. We will perform a validation of the isotropic-viscosity case in the three-field formulation of torsional deformation. This is intended as a verification that there are no problems in the existing code for coupled magma/mantle dynamics, aside from the implementation of viscous anisotropy. The growth rate of porosity perturbations can be calculated as

$$\dot{s} = -C_0 + (1 - \phi_0)\epsilon^{-1}C_1. \quad (80)$$

Here C_0 is the base-state compaction rate and C_1 is the first order compaction rate. $\epsilon = 0.0001$ has been chosen so that the assumptions of linearized stability analysis are still valid. It is

known from theory that in the absence of viscous anisotropy there is no base-state compaction

$$C_0 = 0. \quad (81)$$

In figure 11 the growth rate of spiral-staircase shaped porosity perturbations is plotted as a function of the reference angle with respect to the shear plane at $r = 0.75$. We have $KR = 50$

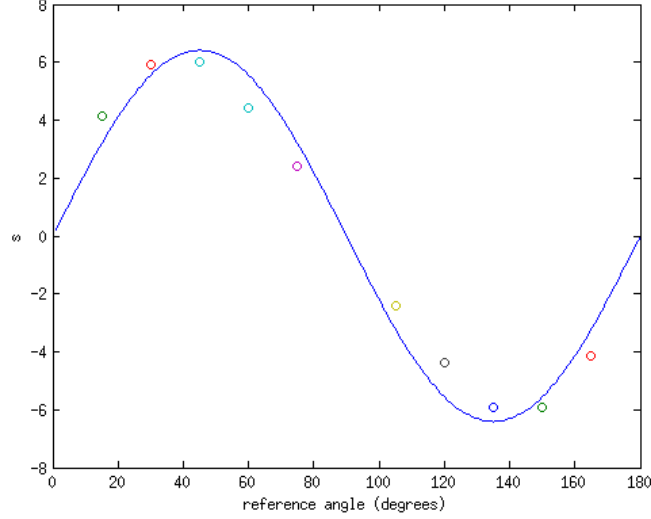


Figure 11: growth rate profile. From left to right the values of K are 5, 8, 8, 8, 10, 10, 8, 8, 8, 5.

in the numerical simulation, though the curve represents the analytical solution for $KR \rightarrow \infty$. Aside from this standard parameter values have been used. The porosity-weakening factor is given by $\lambda = 27.0$. The bulk/shear viscosity ratio is given by $r_\zeta = 5/3$. In figure 12 the growth rate for one value of the reference angle is shown on a slice of the cylinder at $z = .5$. It can be

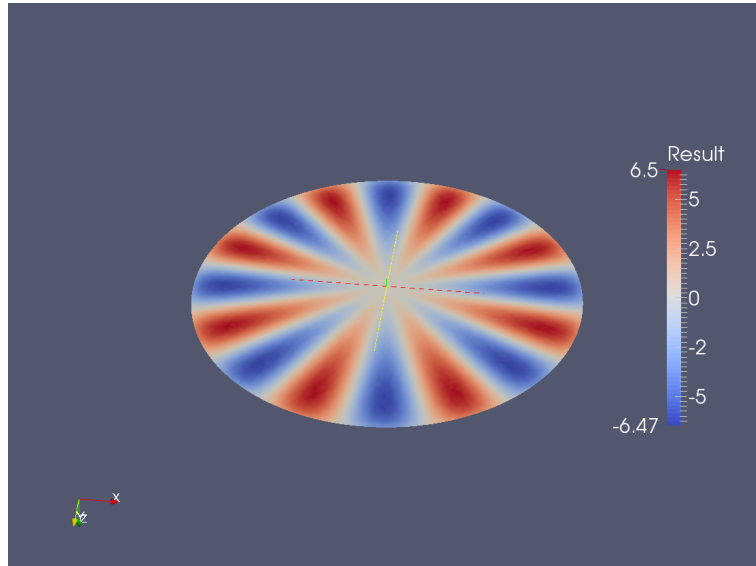


Figure 12: slice of the cylinder at $z = 0.5$. The growth rate of the porosity perturbations is shown. The reference angle is $3.0\pi/12.0$.

seen that the perturbation growth rate goes as we approach the edge of the cylinder. This is a result of the fact that the Dirichlet boundary condition prevents the solid from moving out of

the high-porosity bands. Near the axis of the cylinder the perturbation growth rate also goes to zero. This is a result of the fact that the porosity is ill-resolved there. The smooth curve in figure 11 is (5.26) from Takei and Katz [2013]. It can be seen that the perturbation growth rates that we have found to not fall exactly on this curve. There are several things that may explain the deviation of the data points. One is that (5.26) gives the perturbation growth rate profile for $KR \rightarrow \infty$. The numerical growth rates have been calculated for $KR = 50.0$. Secondly the perturbations are not well-resolved by the mesh for $\theta = \pi/12.0$ and $\theta = 11.0\pi/12.0$. That said, in the 2D simple shear flow case the growth rate becomes smaller as the perturbations become ill-resolved, see the Katz and Takei [2013], and the growth rate here is larger. A third reason for the mismatch is that the growth rates were calculated at a location close to $r = .75$ but not exactly at this radius because Paraview only let us sample the growth rates at specific points on the curve that we determined.

3.6 Secondary flow in the 3D Torsional Flow case

This section is concerned with a secondary flow that develops in the 3D torsional flow simulations (both the two-field and three-field ones) as a result of the truncation of the cylinder. The theory of viscous anisotropy predicts that base-state segregation occurs in 3D torsional flow Takei and Katz [2013]. Base-state segregation is a domain-scale segregation of the solid and the liquid, where the liquid gathers near the axis of the cylinder and the solid is expelled to the outer edge of the cylinder. The simulations in figures 9 and ?? exhibit base-state segregation. However base-state segregation is prevented close the top and bottom boundary of the cylinder due to the use of a Dirichlet boundary condition for the solid velocity there. We have previously shown that the use of Dirichlet boundary conditions at the side boundary of the cylinder only results in a disturbance that is localized to the side wall. The situation for the Dirichlet boundary condition at the top and bottom of the cylinder is different from this. It can be seen that a domain-scale secondary flow is present in the simulations. We think that this is the result of the choice for a Dirichlet boundary condition at the top and bottom of the cylinder with a zero radial velocity solid component. (Any other slice of the cylinder does have a radial velocity component due to base-state segregation.)

We will now describe this secondary flow. Figure 13 illustrates the secondary flow. The

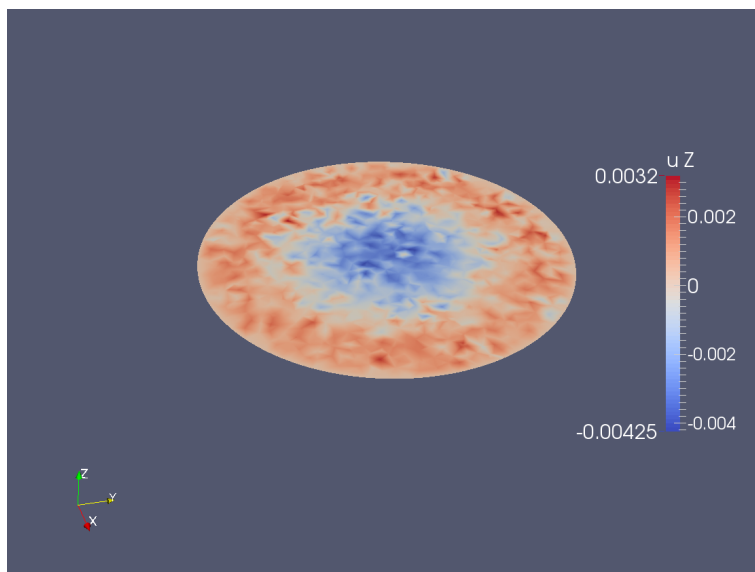


Figure 13: z-component of the secondary flow at $z = .75$ for $\alpha = 2.0$. The number of elements between the axis of the cylinder and the side wall is $N = 20$.

secondary flow moves solid towards the mid-plane at $z = 1/2$ along the axis of the cylinder away from the top and the bottom of the cylinder. At the $z = 1/2$ mid-plane this flow component rolls over. It moves to the side of the cylinder and then it moves along the side-boundary of the domain solid towards the bottom and the top of the cylinder. At the top and the bottom of the cylinder it rolls over again so that it is again in the position from which the solid was moved to the mid-plane of the cylinder. There is also a slight enhancement of the angular velocity component in comparison to the base-state solution.

We will now discuss that the presence of a secondary flow is robust under variation in the boundary conditions and domain. The magnitude of the secondary flow solid velocity component appears to be independent of the length of the cylinder. Furthermore we also have that the position where the rolling-over motion occurs is robust under the choice of boundary condition. The rolling-over motion always occurs at the midpoint between the top and the bottom of the cylinder, even if a boundary condition is chosen where the top of cylinder rotates and the bottom is stationary, as in the experiments Qi et al. [2014].

We will now discuss the implications of this secondary flow. This flow is largely rotation, though we cannot give a precise verification of this statement. It is not possible in the three-field formulation to accurately isolate the secondary flow component for high anisotropy α because of the perturbations. A mostly rotational flow will not affect the compaction rate much. However this secondary flow is still undesirable because we are trying to reproduce a solution that is valid for infinite domains and this secondary flow is not a part of this solution and a possible source of errors. Also the secondary flow might lead to unphysical nonlinear interactions when viscous anisotropy is implemented into the time-stepping code.

We will now consider new boundary conditions that eliminate this secondary flow. As mentioned we expect that this secondary flow is the result of the fact that the radial velocity component at the top and bottom Dirichlet boundary condition is zero. A solution would be to specify the radial velocity component here that is consistent with torsional flow in an infinite cylinder. Unfortunately this is harder than it sounds. There is no explicit expression available for the radial velocity component in 3D torsional flow. The radial velocity component can be determined as the numerical solution of a second order ordinary differential equation (5.7) in Takei and Katz [2013]. We do not know whether FEniCS has features for specifying a set of numerical values at the boundary of a domain instead of an explicit expression. We have not tried this yet. If we examine the radial velocity component at the mid-plane $z = 1/2$ of the cylinder in Paraview then it can be seen that it looks like $0.14 \sin(\pi r)$. Applying this expression at the top and bottom boundary however gives perturbations of size $\hat{1}$. We can tell that it is close to the true radial velocity component because variations give much larger errors. An alternative approach is to apply a periodic BC. However this will still cause a secondary flow, even if there is no rotational motion at the top and the bottom.

In conclusion the torsional flow simulations exhibit a secondary flow that is undesirable when we are comparing the analytical solution for an infinite cylinder to the simulations.

3.7 Perturbations in the three-field 3D torsional flow case

The three-field 3D torsional flow case suffers from nonphysical perturbations for high anisotropy magnitude. These appear at specific places in the cylinder. In this section we will first illustrate the anisotropy-dependence of the perturbations. Then we will consider the places where the perturbations appear and possible causes. Here we also examine the effect of using higher-order elements or a different interpolation order of the viscosity tensor.

We will first illustrate that the perturbations only appear for high values of the anisotropy magnitude. In figure 14 the compaction pressure at $z = .5$ is plotted for $\alpha = 1.3$, $R = 1.0$, $N = 20$. One can see that the profile is smooth. In figure the compaction pressure is plotted

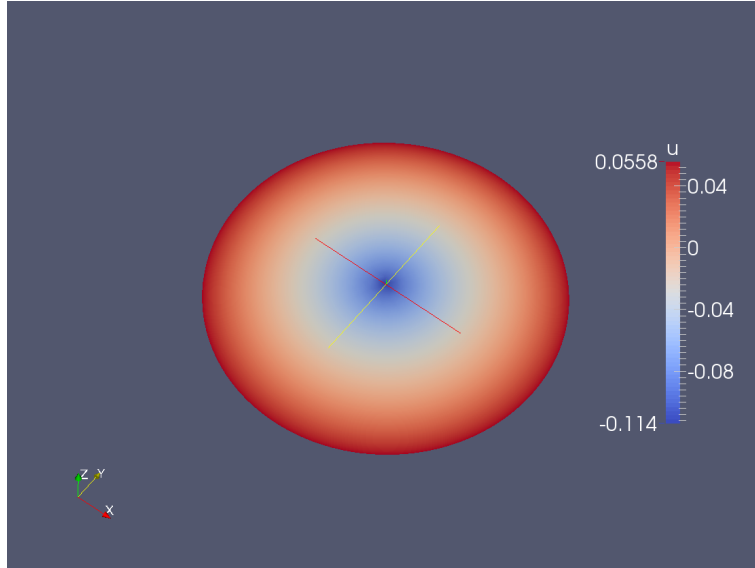


Figure 14: compaction pressure profile for $\alpha = 1.3$.

for $\alpha = 2.0$, $R = 1.0$, $N = 20$. One can see that there are perturbations.

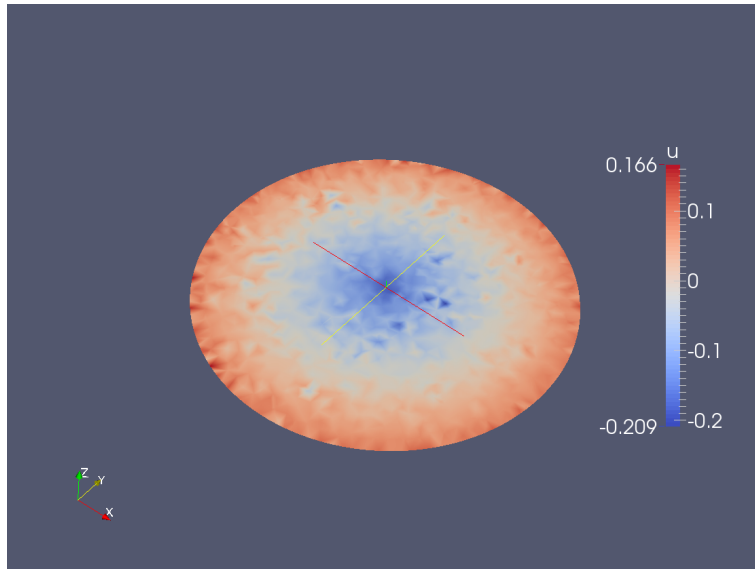


Figure 15: compaction pressure profile for $\alpha = 2.0$.

We think that there are two independent sources of perturbations. There are perturbations that appear along the axis of the cylinder and there are perturbations that appear alongside the side wall. The top and bottom boundary may also have an influence but we have not been able to isolate these. One hypothesis that we have considered is that the interpolation order of the viscosity tensor is insufficient. Before the conservation equations can be solved in a finite-element model it is first necessary to interpolate the viscosity tensor into a finite-element space. The finite-element model that we have usually considered, interpolated the viscosity tensor into a space of piecewise quadratic polynomials. This in effect means that we are solving the conservations not for the actual viscosity tensor but for an approximation of it. Since variations in the viscosity tensor cause physical perturbations, this suggests that numerical variations in the viscosity tensor might cause numerical perturbations. We note in this regard that the 2D simple shear flow problem has a constant viscosity tensor, and a piecewise quadratic interpolation of it is exact. We also note that no perturbations are seen in the simple shear

deformation finite-element model.

As a test of this hypothesis we have implemented a finite-element model with higher-order interpolation of the viscosity tensor. The use of piecewise third order polynomials to interpolate the viscosity tensor indeed gives an improvement. However interpolating the viscosity tensor with fourth-order or fifth-order polynomials gives perturbations with the same extend as before. We also note that using P3-P2-P2 elements gives a vast improvement, even though the perturbations have not dissapeared at the boundary. This indicates that the problem is not only the interpolation of the viscosity tensor but also the solution of the conservation equations for this approximation to the tensor. Finally we note that the perturbations are absent in the two-field formulation of the finite-element model. This shows that there is a numerical instability at work and that the perturbations are not the inevitable consequence of a poor interpolation order. Therefore we consider this hypothesis discredited in itself, though the interpolation order may play a role in inducing numerical instability because the perturbations specifically appear at the boundary and axis of the cylinder where the interpolation order is particularly relevant.

In order to prevent confusion we note here that we have also run simulations with P1-P1-P1 elements (without stablization). The low quality of the interpolation of the velocity terms seemed not to affect the quality of the solution in a simulation with low nondimensional compaction length R , except in that patches of instability would appear. The savings in memory would allow a larger mesh size. However in the torsional simulations with high R the use of P1-P1-P1 elements gives large perturbations. Simulations with low R seem to be prone to instability anyway if the mesh size is large. Therefore we think that this is not a good approach to consider.

Finally we note that the perturbations usually decrease in extend as the mesh size becomes larger, but not for all values of N . For example $N = 32$ gives larger perturbations than $N = 30$, perhaps because the mesh has been modified for cavities. The nondimensional compaction length R also appears to make the perturbations worse if it is ill-resolved by the mesh.

3.7.1 Perturbations at the side wall of the domain

These become visible by humans eye between $\alpha = 1.4$ and $\alpha = 1.5$. In figure 16 the compaction pressure is shown for $\alpha = 1.453$. It can be seen that there are perturbations on the side wall.

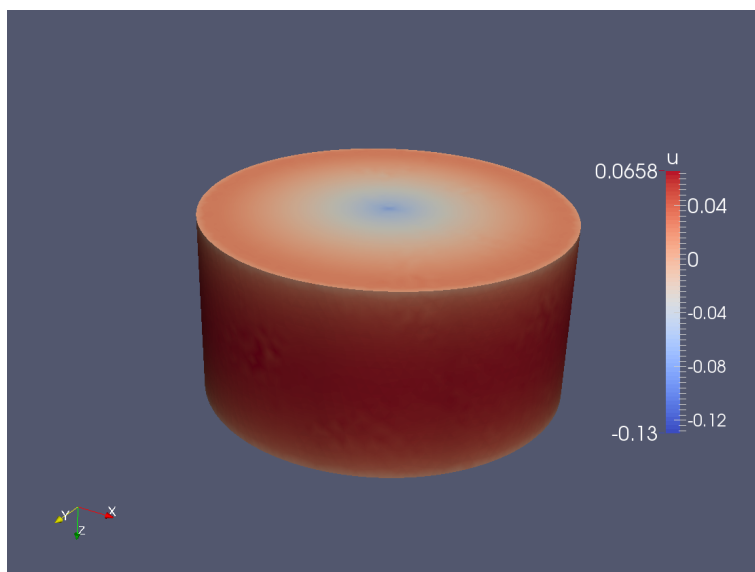


Figure 16: compaction pressure profile at the edge of the domain for $\alpha = 1.453$.

No perturbations propagate much into the domain, and there are no perturbations near the

axis of the cylinder, as can be seen in figure 17. We think the perturbations that we see here are the result of the fact that the curved boundary of the actual cylinder is approximated by a piecewise linear boundary in the simulation. This is a problem, because it does not match the order of the polynomial function space that the viscosity tensor. Unfortunately FEniCS does not have capabilities for applying higher-order polynomial boundaries so this hypothesis cannot be tested directly. That said, use of P3-P2-P2 elements reduces the perturbations at the side wall, even though they do not disappear. Also there are no perturbations at the side wall in the two-field formulation.

3.7.2 Perturbations at the axis of the cylinder

In figure the results of a simulation with anisotropy profile $\alpha = 1.3 + .3(1 - r)$ are shown. It can be seen that perturbations exist near the axis of the cylinder that do not extend to the outer edge. This problem is caused by the fact that under the assumption of fixed anisotropy the components of the anisotropy tensor, which are a function only of ψ , vary rapidly near the axis of the cylinder. This problem cannot be solved since, whatever the grid size, there will always be some small r so that the viscosity tensor is ill-resolved by the mesh. It is however a question to what extent this is a problem. Physically realistic simulations make use of dynamic anisotropy, where the anisotropy magnitude is proportional to the strain rate. The strain rate is roughly proportional to r under torsional deformation. This means that it is unlikely that the anisotropy magnitude in torsional flow is large enough close to the axis to cause perturbations. The perturbations near the axis seem to disappear if P3-P2-P2 elements are used. They also disappear if the two-field formulation is used.

3.7.3 Position-dependent anisotropy magnitude

I will now use the following profile for the anisotropy magnitude

$$\alpha = 8.0 * r * (1.0 - r). \quad (82)$$

This profile ensures that there is no anisotropy near the axis and side boundary, which is known to have a problematic effect on the quality of the solution. However there is still a sizeable region in the domain where the anisotropy magnitude is high. This results in the following compaction pressure profile at the $z = .5$ plane, see figure 19. At the top and the bottom of the cylinder there are still perturbations, as can be seen in figure 20. It turns out that these perturbations are strongly dependent on the mesh size. Therefore I would expect them to diminish considerably as the mesh size increases, and in any case, we are not really interested in the top and the bottom of the cylinder because we are trying to reproduce an analytical solution for an infinite domain.

4 New field-splitting for the three-field formulation

The modified bulk stress balance equation is given by

$$0 = \nabla \left(-\frac{1}{3} \eta_\phi \nabla \cdot \mathbf{u}_s \right) + \nabla \left(\frac{1}{2} \eta_\phi (\nabla \mathbf{u}_f + \nabla \mathbf{u}_f^T) \right) - \nabla p_f - \nabla p_c - \frac{\partial}{\partial x_j} \left(\frac{1}{2} \alpha \eta_\phi a_{ix_g} a_{jx_g} a_{kx_g} a_{lx_g} \dot{\epsilon}_{kl} \right). \quad (83)$$

We introduce a vector-valued fourth field

$$\mathbf{t} = \frac{\partial}{\partial x_j} \left(\frac{1}{2} \alpha \eta_\phi a_{ix_g} a_{jx_g} a_{kx_g} a_{lx_g} \dot{\epsilon}_{kl} \right). \quad (84)$$

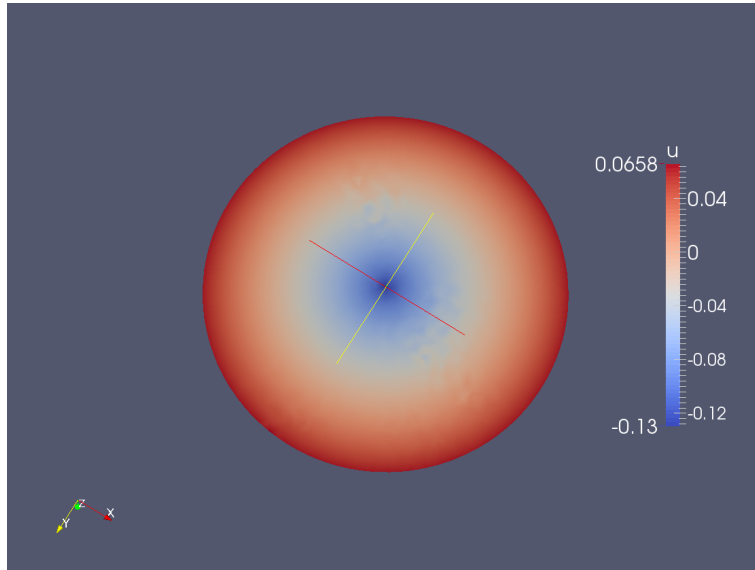


Figure 17: compaction pressure profile on a slice of the cylinder at $z = .5$ for $\alpha = 1.453$.

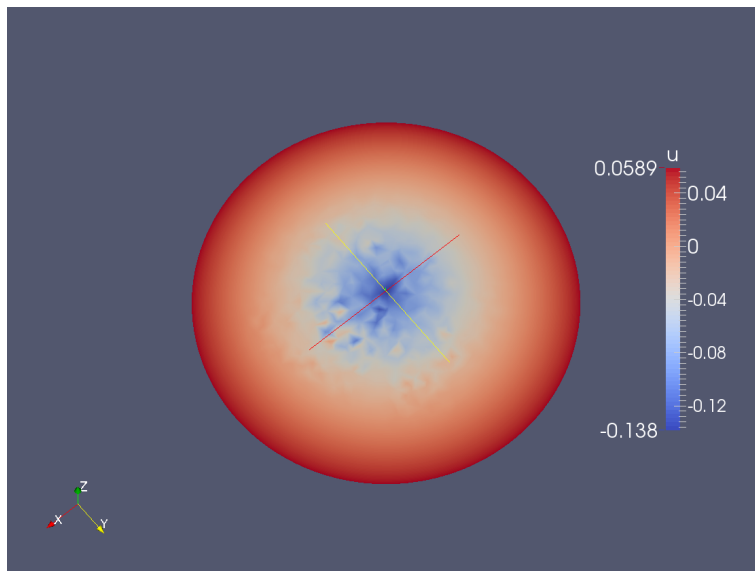


Figure 18: compaction pressure profile at the axis of the cylinder.

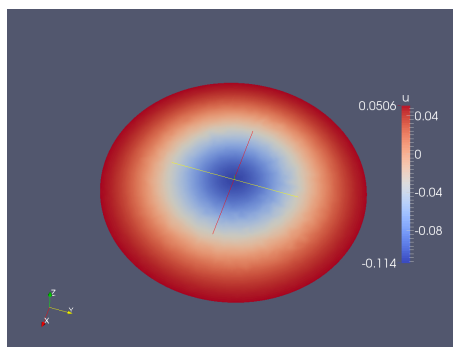


Figure 19: compaction pressure profile on a slice of the cylinder at $z = .5$ for $\alpha = 8.0r(1.0 - r)$.

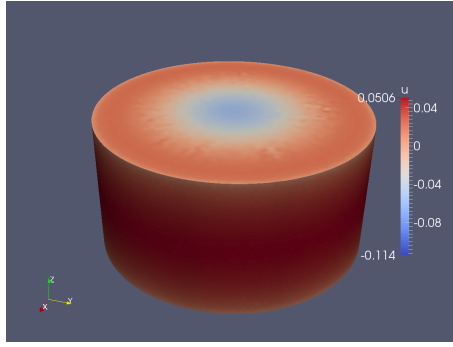


Figure 20: compaction pressure profile at the edge of the cylinder for $\alpha = 8.0r(1.0 - r)$.

The modified bulk stress balance equation then becomes

$$0 = \nabla \left(-\frac{1}{3} \eta_\phi \nabla \cdot \mathbf{u}_s \right) + \nabla \left(\frac{1}{2} \eta_\phi (\nabla \mathbf{u}_f + \nabla \mathbf{u}_f^T) \right) - \nabla p_f - \nabla p_c - \mathbf{t}. \quad (85)$$

The contribution of the new term to the weak formulation of the modified bulk stress balance becomes

$$- \int_{\Omega} \mathbf{t} \cdot \mathbf{v} \, dx. \quad (86)$$

We will now determine the weak formulation of the definition of the vector-valued fourth field 83. We take the inner product with a new vector-valued test function \mathbf{z}

$$\int_{\Omega} \mathbf{t} \cdot \mathbf{z} \, dx = \int_{\Omega} \frac{\partial}{\partial x_j} \left(\frac{1}{2} \alpha \eta_\phi a_{ix_g} a_{jx_g} a_{kx_g} a_{lx_g} \dot{e}_{kl} \right) z_i \, dx. \quad (87)$$

One question is whether we should integrate by parts this integral to lose the second derivative. If we do this then we end up with a boundary term. This might be undesirable. On the other hand, if we do not integrate by parts then it might be needed to use a high-order finite-element space for \mathbf{t} and \mathbf{z} . This is expensive in memory and CPU capacity. An alternative is to replace the scalar-valued p_c by a tensor valued third field and to include the anisotropy term in this new field definition. However this will be expensive in memory and CPU capacity.

5 Conclusion

In this report anisotropic viscosity was implemented into a finite element model for coupled magma/mantle dynamics. Two formulations of the conservation equations were considered. The conservation equations for simple shear deformation and torsional deformation apply a different viscosity tensor. That is why we will discuss them separately.

First we will discuss the two-field formulation for simple shear deformation. It is our impression that anisotropic viscosity has been implemented correctly into the two-field formulation for simple shear deformation, where the conservation equations are considered in their original form. The reasons for believing so are that the perturbation growth rate curve for saturated anisotropy has been correctly reproduced by the finite element model for the three-field formulation. This is of course not the two-field formulation, but for saturated anisotropy, and when a direct solver is used for solving the direct system, there is no reason to believe that the three-field formulation should give incorrect answers. In addition the perturbation growth rate has been correctly reproduced by the finite element model for the two-field formulation for a single perturbation angle. Testing indicates that the preconditioner that has been modified for anisotropy works very well.

We will now discuss the three-field formulation for torsional deformation. Unfortunately the finite element model for the two-field formulation is not good enough to perform time-dependent simulations. The reason for this is that numerical instability can occur at very low values of the porosity. This is the reason that the three-field formulation has been developed, where a variable named the compaction pressure is introduced to eliminate a grad-div term. Implementation of viscous anisotropy into the three-field formulation is problematic because the velocity block in the system matrix becomes indefinite at anisotropy magnitude $\alpha \approx 1.37$, a phenomenon that does not occur for the two-field formulation. Examination of the modified conservation equations in grain coordinates shows that they lose the property of ellipticity for $\alpha > 4/3$. In cartesian coordinates the magnitude of the largest component in the viscosity tensor decreases. The loss of ellipticity is a problem irrespective of the solution method that is used because the system matrix is then expected to become singular at $\alpha \approx 4/3$. This is an unacceptable situation under dynamic anisotropy, where the anisotropy magnitude is expected to have a broad range of values over the domain. In addition it prevents the successful functioning of the preconditioner that has been modified for viscous anisotropy, because the velocity block of the preconditioner matrix cannot be approximately inverted by the multigrid algorithm if it is indefinite. The standard preconditioner can be used, though there seems to be a spike in the number of iterations at $\alpha \approx 1.7$, an observation that we cannot immediately explain, and the performance is in any case poor. Aside from this issue of the loss of ellipticity the implementation seems to be correct, because, as mentioned above, the perturbation growth rate curve has been correctly reproduced for saturated anisotropy $\alpha = 2.0$. As mentioned above the loss of ellipticity has been established in grain coordinates. However the finite element model has been expressed in cartesian coordinates. In that case the individual components of the viscosity tensor become smaller and we do not know whether it can still be established whether ellipticity is lost. A closer look at this would be desirable. One way to remove the numerical instability caused by the grad-div terms while leaving the ellipticity intact is to look at alternative field splittings. There are several ways these could be implemented. An easy way is to replace the compaction pressure by a tensor-valued third field, but this is unacceptably expensive in memory and CPU capacity. A more efficient field-splitting uses a vector-valued fourth field. Unfortunately it can be seen right away that there are questions related to the choice of the finite element space for this new function, and whether the resulting boundary term is problematic. This will probably require considerable further study.

We will now discuss the three-field formulation for 3D torsional deformation. Unfortunately this finite element model suffers from numerical instability. We have three reasons for concluding that this instability is numerical in origin. The first reason is that a single test with the two-field formulation for 3D torsional deformation reproduces the same solution but without nonphysical perturbations. The second reason is that the extent and magnitude of the perturbations is sensitive to the mesh size and the order of the elements. The perturbations are considerably smaller if P3-P2-P2 elements are used instead of P2-P1-P1 elements. The third reason for believing that the implementation of viscous anisotropy is physically correct is that the underlying solution beneath the numerical perturbations has qualitative features that are correct. In particular the base-state compaction results match the analytical results fairly well for nondimensional compaction length $R = 1$ and $R = 0.1$. There is a deviation at the axis of the cylinder that is a result of the ill-resolvedness of the porosity. Slight numerical differences at other points of the domain may be the result of the existence of a secondary flow.

We will now discuss the two-field formulation for 3D torsional flow. As mentioned above the two-field formulation for 3D torsional flow does not suffer from numerical perturbations. This has been established in a single test. One of the first things that need to be done in the future is a formal validation for 3D torsional flow where the perturbation growth rate curve is reproduced using a two-step approach. This will provide additional confirmation that the implementation

of viscous anisotropy in 3D torsional flow is correct from a physical standpoint. One thing that is worrisome is that when the modified preconditioner is used to calculate the solution iteratively the relative residual gets stuck at $e - 5$ even though the preconditioned residual quickly converges to machine precision. We cannot explain this at this point. The solution looks the same as when a direct solver is applied. Unfortunately the two-field formulation is not good enough for time-dependent simulations, because of a numerical instability that occurs for very low values of the porosity. This is why the three-field formulation has been developed. We cannot explain at this point why the numerical perturbations occur for the three-field formulation but not for the two-field formulation. Unlike simple shear deformation, the velocity block remains positive definite for anisotropy values for all physical values of the anisotropy magnitude. We do not know whether the conclusion about loss of ellipticity in grain coordinates can be extended to torsional flow, where the anisotropy direction is dependent on the position, and the components of the viscosity tensor are generally smaller as a result. Generally speaking it is known from the numerical analysis literature that Stokes flow is prone to numerical instability. One property related to this inf-sup instability. It might be a good idea to prove inf-sup instability for the modified conservation equations. As a final remark we mention that the numerical perturbations occur at particular places in the domain. They independently appear at the outer edge of the domain at $\alpha \approx 1.4$ and the axis of the cylinder at $\alpha \approx 1.6$. This is hypothesized to be a result of the ill-resolvedness of the viscosity tensor near the axis of the cylinder under fixed anisotropy, and the poor approximation quality of the piecewise linear approximation to the curved boundary. Higher order approximations to curved boundaries are currently not implemented in FEniCS. Tests indicate that there also other factors that affect the extend of the perturbations such as R , the mesh size N and even an inappropriate implementation of the boundary conditions. This suggests that my description of the parameter-dependencies of the perturbations at the outer edge and the axis is likely to be incomplete. We are not hopeful that the cause of the perturbations can be found by further variation of the parameters. We would focus on the fact that the perturbations are absent in the two-field formulation and examine the literature for properties of the modified conservation equations that relate to stability.

We will make a final remark related to the original purpose of this project of further validation of the theory of viscous anisotropy. The problem in the original torsion simulations as reported in Katz and Takei [2013] is that a cylindrical coordinate system is used and that the variable mesh sizing leads to a bias in the perturbation growth rate at small radii. The perturbations growth rates there are too high. It is dubious whether the use of cartesian coordinates really solves this problem. The ill-resolvedness of the porosity perturbations near the axis of the cylinder is expected to lead to perturbation growth rates that are too low. Finally new boundary conditions at the top and bottom of the cylinder must be found that prevent the secondary flow from forming. It would also be desirable to implement the boundary conditions from Takei and Katz [2013] at the side wall, but this is not expected to be essential.

Finally we note that after implementation of dynamic anisotropy, and after solution of the problems related to the loss of ellipticity and numerical instability, the code would also be very fast solver for magma/mantle dynamics in subduction zones, as described in Spiegelman [2003].

References

- L. Alisic, J. Rudge, R. Katz, G. Wells, and S. Rhebergen. Compaction around a rigid, circular inclusion in partially molten rock. *Unpublished research*, 2013.
- S. Brenner and R. Scott. *The mathematical theory of finite element methods*, volume 15. Springer, 2008.

- J. Freund and R. Stenberg. On weakly imposed boundary conditions for second order problems. In *Proceedings of the Ninth Int. Conf. Finite Elements in Fluids*, pages 327–336, 1995.
- R. Katz and M. Spiegelman. An introduction to coupled magma/mantle dynamics. *lecture notes*, 2013.
- R. Katz and Y. Takei. Consequences of viscous anisotropy in a deforming, two-phase aggregate: 2. Numerical solutions of the full equations. *J. Fluid Mech.*, 734:456–485, 2013. doi: 10.1017/jfm.2013.483.
- P. Kundu, I. Cohen, and D. Dowling. *Fluid Mechanics Fifth Edition*. Academic Press, 2011.
- A. Logg, K. Mardal, and G. Wells. *Automated solution of differential equations by the finite element method*. Springer, 2012.
- D. McKenzie. The generation and compaction of partially molten rock. *J. Petrol.*, 25, 1984.
- C. Qi, Y. Zhao, and D. Kohlstedt. An experimental study of pressure shadows in partially molten rocks. *Earth Plan. Sci. Lett.*, 382:77–84, 2013.
- C. Qi, D. Kohlstedt, R. Katz, and Y. Takei. An experimental test of the viscous anisotropy hypothesis for partially molten rocks. *Unpublished research*, 2014.
- S. Rhebergen, G. Wells, A. Wathen, R. Katz, A. L, and R. JF. Optimal three-field block-preconditioners for models of coupled magma/mantle dynamics. *unpublished research*, 2014.
- M. Spiegelman. Linear analysis of melt band formation by simple shear. *Geochem. Geophys. Geosys.*, 2003. doi: 10.1029/2002GC000499.
- Y. Takei and R. Katz. Consequences of viscous anisotropy in a deforming, two-phase aggregate: 1. Governing equations and linearised analysis. *J. Fluid Mech.*, 734:424–455, 2013. doi: 10.1017/jfm.2013.482.

A Derivation of weak formulation for the elliptic equations

We start with the equation

$$\nabla \cdot (-k_\phi \nabla p_f + \mathbf{u}_s) = 0. \quad (88)$$

Multiply by a test function q and integrate over the domain Ω

$$\int_{\Omega} \nabla \cdot (-k_\phi \nabla p_f + \mathbf{u}_s) q \, dx = 0. \quad (89)$$

Apply integration by parts to the pressure gradient term

$$\int_{\Omega} k_\phi \nabla p_f \cdot \nabla q + \nabla \cdot \mathbf{u}_s q \, dx - \int_{\partial\Omega} k_\phi \nabla p_f \cdot \hat{\mathbf{n}} q \, ds. \quad (90)$$

Now consider the equation

$$\nabla \cdot (\eta_\phi \mathbf{D}\mathbf{u}_s) + \nabla \cdot \left(\left(\zeta_\phi - \frac{1}{3} \eta_\phi \right) \nabla \cdot \mathbf{u}_s \right) - \nabla p - [\alpha(1/2) a_{i1} a_{j1} a_{k1} a_{l1} \eta_\phi \dot{\epsilon}_{kl}]_{,j} = 0. \quad (91)$$

These are actually three equations. Take the inner product with a vector-valued test function \mathbf{v} and integrate over the domain Ω

$$\int_{\Omega} \nabla \cdot (\eta_{\phi} \mathbf{D}\mathbf{u}_s) \cdot \mathbf{v} + \nabla \cdot ((\zeta_{\phi} - \frac{1}{3}\eta_{\phi}) \nabla \cdot \mathbf{u}_s) \cdot \mathbf{v} - \nabla p \cdot \mathbf{v} - [\alpha(1/2)a_{i1}a_{j1}a_{k1}a_{l1}\eta_{\phi}\dot{\epsilon}_{kl}]_{,j} v_i \, dx = 0. \quad (92)$$

I will now integrate by parts these terms individually. For the first term we first switch to indicial notation

$$\int_{\Omega} \nabla \cdot (\eta_{\phi} \mathbf{D}\mathbf{u}_s) \cdot \mathbf{v} \, dx = \int_{\Omega} \frac{\partial}{\partial x_j} (\eta_{\phi} \frac{1}{2} (\frac{\partial u_i^s}{\partial x_j} + \frac{\partial u_j^s}{\partial x_i})) v_i \, dx \quad (93a)$$

$$= - \int_{\Omega} (\eta_{\phi} \frac{1}{2} (\frac{\partial u_i^s}{\partial x_j} + \frac{\partial u_j^s}{\partial x_i})) \frac{\partial v_i}{\partial x_j} \, dx + \int_{\partial\Omega} \eta_{\phi} \frac{1}{2} (\frac{\partial u_i^s}{\partial x_j} + \frac{\partial u_j^s}{\partial x_i}) v_i \nu_j \, ds \quad (93b)$$

$$= - \int_{\Omega} \eta_{\phi} \frac{1}{2} (\frac{\partial u_i^s}{\partial x_j} + \frac{\partial u_j^s}{\partial x_i}) \frac{1}{2} (\frac{\partial v_j^s}{\partial x_i} + \frac{\partial v_i^s}{\partial x_j}) \, dx + \int_{\partial\Omega} \eta_{\phi} \frac{1}{2} (\frac{\partial u_i^s}{\partial x_j} + \frac{\partial u_j^s}{\partial x_i}) v_i \nu_j \, ds \quad (93c)$$

$$= - \int_{\Omega} \eta_{\phi} \mathbf{D}\mathbf{u}_s : \mathbf{D}\mathbf{v} \, dx + \int_{\partial\Omega} \frac{1}{2} \mathbf{v} \cdot \mathbf{D}\mathbf{u}_s \cdot \hat{\mathbf{n}} \, ds \quad (93d)$$

I will now apply integration by parts to the compaction stress term

$$\int_{\Omega} \nabla \cdot ((\zeta_{\phi} - \frac{1}{3}\eta_{\phi}) \nabla \cdot \mathbf{u}_s) \cdot \mathbf{v} \, dx = - \int_{\Omega} (\zeta_{\phi} - \frac{1}{3}\eta_{\phi}) \nabla \cdot \mathbf{u}_s \nabla \cdot \mathbf{v} \, dx \quad (94a)$$

$$+ \int_{\partial\Omega} (\zeta_{\phi} - \frac{1}{3}\eta_{\phi}) \nabla \cdot \mathbf{u}_s \mathbf{v} \cdot \hat{\mathbf{n}} \, ds. \quad (94b)$$

Next I will work out the pressure gradient term

$$\int_{\Omega} \nabla p \cdot \mathbf{v} \, dx = - \int_{\Omega} p \nabla \cdot \mathbf{v} \, dx \quad (95a)$$

$$+ \int_{\partial\Omega} p \mathbf{v} \cdot \hat{\mathbf{n}} \, ds \quad (95b)$$

Finally I will apply integration by parts to the anisotropy term

$$\int_{\Omega} [\alpha(1/2)a_{i1}a_{j1}a_{k1}a_{l1}\eta_{\phi}\dot{\epsilon}_{kl}]_{,j} v_i \, dx = - \int_{\Omega} [\alpha(1/2)a_{i1}a_{j1}a_{k1}a_{l1}\eta_{\phi}\dot{\epsilon}_{kl}] v_{i,j} \, dx \quad (96a)$$

$$+ \int_{\partial\Omega} [\alpha(1/2)a_{i1}a_{j1}a_{k1}a_{l1}\eta_{\phi}\dot{\epsilon}_{kl}] v_i \, ds. \quad (96b)$$

A.1 Boundary terms

I will now simplify all the boundary terms we have found previously as much as possible.

A.1.1 Term arising from the compaction equation

For the first term we have that all walls of the flow domain are impermeable to the liquid and hence the following boundary condition holds

$$-k_{\phi} \nabla p \cdot \hat{\mathbf{n}} = 0 \quad (97)$$

We then find

$$- \int_{\partial\Omega} k_{\phi} \nabla p \cdot \hat{\mathbf{n}} \, ds = 0. \quad (98)$$

A.1.2 Terms arising from the stress balance for the liquid + matrix

I will first consider the term

$$\int_{\partial\Omega} \frac{1}{2} \mathbf{v} \cdot \mathbf{D}\mathbf{u}_s \cdot \hat{\mathbf{n}} \, ds. \quad (99)$$

We have Dirichlet conditions at all walls. We therefore look in a space of test functions with $\mathbf{v} = \mathbf{0}$ on all the walls. We then find

$$\int_{\partial\Omega} \frac{1}{2} \mathbf{v} \cdot \mathbf{D}\mathbf{u}_s \cdot \hat{\mathbf{n}} \, ds = 0. \quad (100)$$

For the same reason the compaction stress term drops out

$$\int_{\partial\Omega} (\zeta_\phi - \frac{1}{3}\eta_\phi) \nabla \cdot \mathbf{u}_s \mathbf{v} \cdot \hat{\mathbf{n}} \, ds = 0. \quad (101)$$

and the boundary term for the pressure

$$\int_{\partial\Omega} p \mathbf{v} \cdot \hat{\mathbf{n}} \, ds = 0. \quad (102)$$

Finally, because of the Dirichlet condition on the boundary the anisotropy term drops out

$$\int_{\partial\Omega} [\alpha(1/2)a_{i1}a_{j1}a_{k1}a_{l1}\eta_\phi\dot{e}_{kl}] v_i n_i \, ds = 0. \quad (103)$$

B Implementation of the boundary conditions for torsional flow from Takei and Katz [2013]

In this section a few notes are given on how to implement the boundary conditions for torsional flow from Takei and Katz [2013]. As mentioned in section 2.3 we have identified two ways to do this. The first involves only a small modification of the weak formulation in 2.4. The disadvantage is that implementing it in FEniCS requires a functionality that is not currently available in FEniCS. The second method should not be problematic in FEniCS but will require a considerable amount of analysis. We will first describe the first method.

Finite element models are based on a weak formulation of the field equations and the boundary conditions. The weak formulation for the boundary conditions from Takei and Katz [2013] is largely the same as the one described in section 2.4. In that weak formulation all boundary terms resulting from integration by parts drop out in the weak formulation of the bulk stress balance and the compaction equation in torsional flow with a Dirichlet boundary condition for the velocity at the side wall. This is no longer the case if the boundary conditions for the velocity at the side wall from Takei and Katz [2013] are applied. We will re-examine all boundary terms in the following. Integration by parts of the inner product of the gradient of the shear strain rate and the test function results in the following boundary term

$$\int_{\partial\Omega} \frac{1}{2} \mathbf{v} \cdot \mathbf{D}\mathbf{u}_s \cdot \hat{\mathbf{n}} \, ds. \quad (104)$$

A Dirichlet boundary condition is specified for the velocity at the top and the bottom of the cylinder. This means that the space of test functions will be restricted by the condition that $\mathbf{v} = \mathbf{0}$ there. This implies that the integrand in the boundary term 104 is zero on the top and

the bottom of the cylinder. On the side boundary of the cylinder the contraction product of the shear strain rate tensor and the unit normal vector is given in cylindrical coordinates by

$$\mathbf{D}\mathbf{u}_s \cdot \hat{\mathbf{n}} = \begin{bmatrix} \frac{\partial u_r^s}{\partial r} \\ \frac{r}{2} \frac{\partial(u_\psi^s/r)}{\partial r} + \frac{1}{2r} \frac{\partial u_r^s}{\partial \psi} \\ \frac{1}{2} \left(\frac{\partial u_r^s}{\partial z} + \frac{\partial u_z^s}{\partial r} \right) \\ \cdot \end{bmatrix} \quad (105)$$

The boundary condition $u_{z,r}^s = 0$ immediately implies that $\frac{\partial u_z^s}{\partial r} = 0$. The boundary condition that the velocity component normal to the wall is zero everywhere implies that $\frac{\partial u_r^s}{\partial z} = 0$. It is then found that

$$\mathbf{v} \cdot \mathbf{D}\mathbf{u}_s \cdot \hat{\mathbf{n}} = v_r \frac{\partial u_r^s}{\partial r} + v_\psi \left(\frac{r}{2} \frac{\partial(u_\psi^s/r)}{\partial r} + \frac{1}{2r} \frac{\partial u_r^s}{\partial \psi} \right). \quad (106)$$

The boundary condition that the velocity component normal to the wall is zero everywhere implies that the space of test functions is restricted by the condition $\mathbf{v} \cdot \hat{\mathbf{n}} = 0$. This can also be written as $v_r = 0$. The first term in 106 then drops out. The remaining term can be simplified further. The fact that the normal velocity component is zero on the entire side wall implies that $\frac{1}{2r} \frac{\partial u_r^s}{\partial \psi} = 0$. Furthermore the boundary condition $u_{\psi,r} = z - 1/2$ can be applied. It is found that

$$\frac{r}{2} \frac{\partial u_\psi^s}{\partial r} + \frac{1}{2r} \frac{\partial u_r^s}{\partial \psi} \quad (107a)$$

$$= \frac{r}{2} \left(\frac{-u_\psi^s}{r^2} + \frac{\partial u_\psi^s}{\partial r} \frac{1}{r} \right) \quad (107b)$$

$$= \frac{-u_\psi^s}{2r} + \frac{1}{2} \left(z - \frac{1}{2} \right). \quad (107c)$$

We will now consider the other boundary terms. The Dirichlet boundary condition $u_r = 0$ implies that the space of test functions is restricted by the condition v_ϕ . It is then found that the boundary terms resulting from integration by parts of the other terms in the bulk stress balance are zero.

$$\int_{\partial\Omega} \left(\zeta_\phi - \frac{1}{3} \eta_\phi \right) \nabla \cdot \mathbf{u}_s \mathbf{v} \cdot \hat{\mathbf{n}} \, ds = 0, \quad (108a)$$

$$\int_{\partial\Omega} p \mathbf{v} \cdot \hat{\mathbf{n}} \, ds = 0, \quad (108b)$$

$$\int_{\partial\Omega} [\alpha(1/2) a_{i1} a_{j1} a_{k1} a_{l1} \eta_\phi \dot{e}_{kl}] v_i n_i \, ds = 0. \quad (108c)$$

In conclusion the weak formulation involves one additional boundary term compared to 2.4. Also, the essential boundary condition at the side wall has changed. It is now given by $\mathbf{u}_s \cdot \hat{\mathbf{n}} = 0$. Boundary conditions of this form are not currently implemented in FEniCS. It is implemented by the function *SlipBC* in the Unicorn software library that is a part of the FEniCS framework. We expect that this function can be implemented to work directly in DOLFIN but this might require a considerable amount of time of debugging. Another aspect of this problem that is important for implementation is that different boundary conditions are applied at the top/bottom of the cylinder and the side wall. This means that it is necessary

to mark parts of the boundary. An example of how to do this in the c++ version of FEniCS can be found in the *FEniCS/src/dolphin-1.4.0/demo/undocumented/lift-drag/cpp* folder in the FEniCS installation.

As mentioned there is an alternative method to apply the boundary conditions in Takei and Katz [2013]. This method will require a considerable amount of further analysis before it can be implemented. It consists of applying a Nitsche-type method as described in Freund and Stenberg [1995] to the McKenzie equations with anisotropic viscosity. This will require a major modification of the weak formulation. This method does not involve any essential boundary conditions. As remarked in 3.7 the three-field formulation of the 3D torsional flow problem is sensitive to the numerical perturbations. These perturbations are large at the side wall boundary and it is hypothesized that this is a result of the piecewise linear approximation of the curved boundary. This approximation is rougher than the approximation that is applied on the inside of the domain. Piecewise quadratic interpolation is applied to the velocity fields and viscosity tensor. The absence of essential boundary conditions when applying a Nitsche-type method may reduce the magnitude of perturbations at the boundary. It should be noted that this is pure speculation at this point. It is however suggestive to note that the numerical instability does not seem to apply to the liquid pressure in the three-field formulation. The liquid pressure is smooth. It is noted that the boundary condition for the liquid pressure is a Neumann boundary condition. A disadvantage of the Nitsche-type method is that it may also require a considerable modification of the preconditioner, since there is an extensive modification of the weak formulation.

In conclusion there are possibilities for implementing the boundary conditions from Takei and Katz [2013]. It is also noted that these require a considerable time investment to implement. Therefore the work on implementation of the boundary conditions from Takei and Katz [2013] has been abandoned and a Dirichlet boundary condition is applied in the remainder of this report.

C Derivation of conservation equations

C.1 Conservation of momentum

Microscopically at the scale of grains and pores the solid and liquid phases exist at different positions in space. At the continuum scale however the bulk aggregate is modeled by concurrently existing solid and liquid phases, that permeate the entirety of space and that have densities $\rho_m(1 - \phi)$ and $\rho_f\phi$ respectively. Conservation of momentum for the solid phase is then written

$$\frac{d}{dt} \int_{RVE} \rho_m(1 - \phi) \mathbf{u}_f \, dx = 0. \quad (109)$$

Expanding this derivative

$$\int_{RVE} \frac{\partial \rho_m(1 - \phi) \mathbf{u}_f}{\partial t} \, dx + \int_{\partial RVE} \rho_m(1 - \phi) \mathbf{u}_f \mathbf{u}_f \cdot \hat{\mathbf{n}} \, dx \quad (110a)$$

$$= \int_{RVE} \rho_m(1 - \phi) \mathbf{g} \, dx + \int_{RVE} \mathbf{I} \, dx + \int_{\partial RVE} (1 - \phi) \sigma_{ij}^s \cdot \hat{\mathbf{n}} \, dx. \quad (110b)$$

The term $(1 - \phi) \sigma_{ij}^s$ is the stress density within the solid phase. The motivation for writing it like this is that $1 - \phi$ is the volume fraction of the solid phase and we can then see σ_{ij}^s as the microscopic solid stress tensor averaged over the solid fraction of the local domain.

The solidflows very slowly. Therefore the Reynolds number is very low and we can neglect the inertia terms. The resulting equation is therefore a statement of force balance. After applying Gauss' theorem

$$-(1 - \phi)\rho_m g \delta_{i3} + I_i + \frac{\partial [(1 - \phi)\sigma_{ij}^s]}{\partial x_j}. \quad (111)$$

For the liquid the statement of force balance becomes

$$-\phi\rho_f g \delta_{i3} - I_i + \frac{\partial \phi\sigma_{ij}^f}{\partial x_j} = 0. \quad (112)$$

Microscopically at the level of individual grains and pores the liquid is incompressible. However, at the aggregate level it is modeled as an incompressible fluid. It has a very low liquid shear and liquid bulk viscosity however and is therefore regarded as being unable to sustain any shear and volumetric stresses. This results in the following stress tensor for the liquid phase

$$\sigma_{ij}^f = -p_f \delta_{ij}. \quad (113)$$

Microscopically at the level of individual grains and pores the matrix is incompressible. Macroscopically, at the aggregate level, it is modeled as a compressible fluid that can sustain shear and volumetric stresses. If the matrix is at rest then the stress must be given by the thermodynamic pressure. In the absence of surface tension the microscopic pressure in the liquid and the solid must be the same, or there would be a stress discontinuity at the interface between the liquid and the solid grains. This means that the thermodynamic pressure in the liquid must coincide with that in the matrix. Macroscopically, at the aggregate level the matrix can sustain shear and volumetric stresses. The most general way of relating these to the shear and volumetric strains of the matrix is through a fourth-order viscosity tensor

$$\sigma_{ij}^s = -p_f \delta_{ij} + C_{ijkl} \dot{\epsilon}_{kl} \quad (114)$$

The interphase force is defined to be

$$\mathbf{I} = C_1(\mathbf{u}_f - \mathbf{u}_s) - p_f \nabla \phi. \quad (115)$$

Defining it in this way gives it the following important properties.

The second porosity-gradient term is there to ensure that that only gradients in the liquid pressure cause a segregation flux. If it were not present then also porosity gradients could cause segregation. This would be physically unrealistic. I cannot give a microscopic physical interpretation of this term.